



Programmable antivirals targeting critical conserved viral RNA secondary structures from influenza A virus and SARS-CoV-2

Rachel J. Hagey^{1,2,3}, Menashe Elazar^{1,3}, Edward A. Pham^{1,3}, Siqi Tian⁴, Lily Ben-Avi³, Claire Bernardin-Souibgui³, Matthew F. Yee³, Fernando R. Moreira⁵, Meirav Vilan Rabinovitch³, Rita M. Meganck⁵, Benjamin Fram³, Aimee Beck⁶, Scott A. Gibson⁷, Grace Lam³, Josephine Devera³, Wipapat Kladwang⁴, Khanh Nguyen³, Anming Xiong³, Steven Schaffert⁸, Talia Avisar³, Ping Liu³, Arjun Rustagi⁶, Carl J. Fichtenbaum⁹, Phillip S. Pang³, Purvesh Khatri⁸, Chien-Te Tseng^{10,11}, Jeffery K. Taubenberger¹², Catherine A. Blish^{6,13}, Brett L. Hurst⁷, Timothy P. Sheahan⁵, Rhiju Das^{4,14} and Jeffrey S. Glenn^{1,2,3,15} ✉

Influenza A virus's (IAV's) frequent genetic changes challenge vaccine strategies and engender resistance to current drugs. We sought to identify conserved and essential RNA secondary structures within IAV's genome that are predicted to have greater constraints on mutation in response to therapeutic targeting. We identified and genetically validated an RNA structure (packaging stem-loop 2 (PSL2)) that mediates in vitro packaging and in vivo disease and is conserved across all known IAV isolates. A PSL2-targeting locked nucleic acid (LNA), administered 3 d after, or 14 d before, a lethal IAV inoculum provided 100% survival in mice, led to the development of strong immunity to rechallenge with a tenfold lethal inoculum, evaded attempts to select for resistance and retained full potency against neuraminidase inhibitor-resistant virus. Use of an analogous approach to target SARS-CoV-2, prophylactic administration of LNAs specific for highly conserved RNA structures in the viral genome, protected hamsters from efficient transmission of the SARS-CoV-2 USA_WA1/2020 variant. These findings highlight the potential applicability of this approach to any virus of interest via a process we term 'programmable antivirals', with implications for antiviral prophylaxis and post-exposure therapy.

IAV is a segmented RNA virus that causes major morbidity and mortality worldwide. Current antiviral therapies target viral proteins that frequently mutate, rendering many such therapies inadequate^{1–3}. Despite a breadth of knowledge about the viral life-cycle, knowledge of the RNA secondary structure of the genome is limited. Research on other RNA viruses has revealed genomic RNA to be capable of playing many important roles in viral life-cycles beyond merely encoding amino acid sequences, suggesting that viral RNA structural elements could be promising therapeutic targets^{4,5}. To the extent that these RNA structural elements are both essential and highly conserved, these features could reduce the degree of freedom for mutations that are compatible with virus function. This, in turn, could translate into a high barrier for resistance to therapeutics designed to disrupt these RNA structures. In IAV, genome packaging is one such critical juncture in which RNA structure might serve a central function.

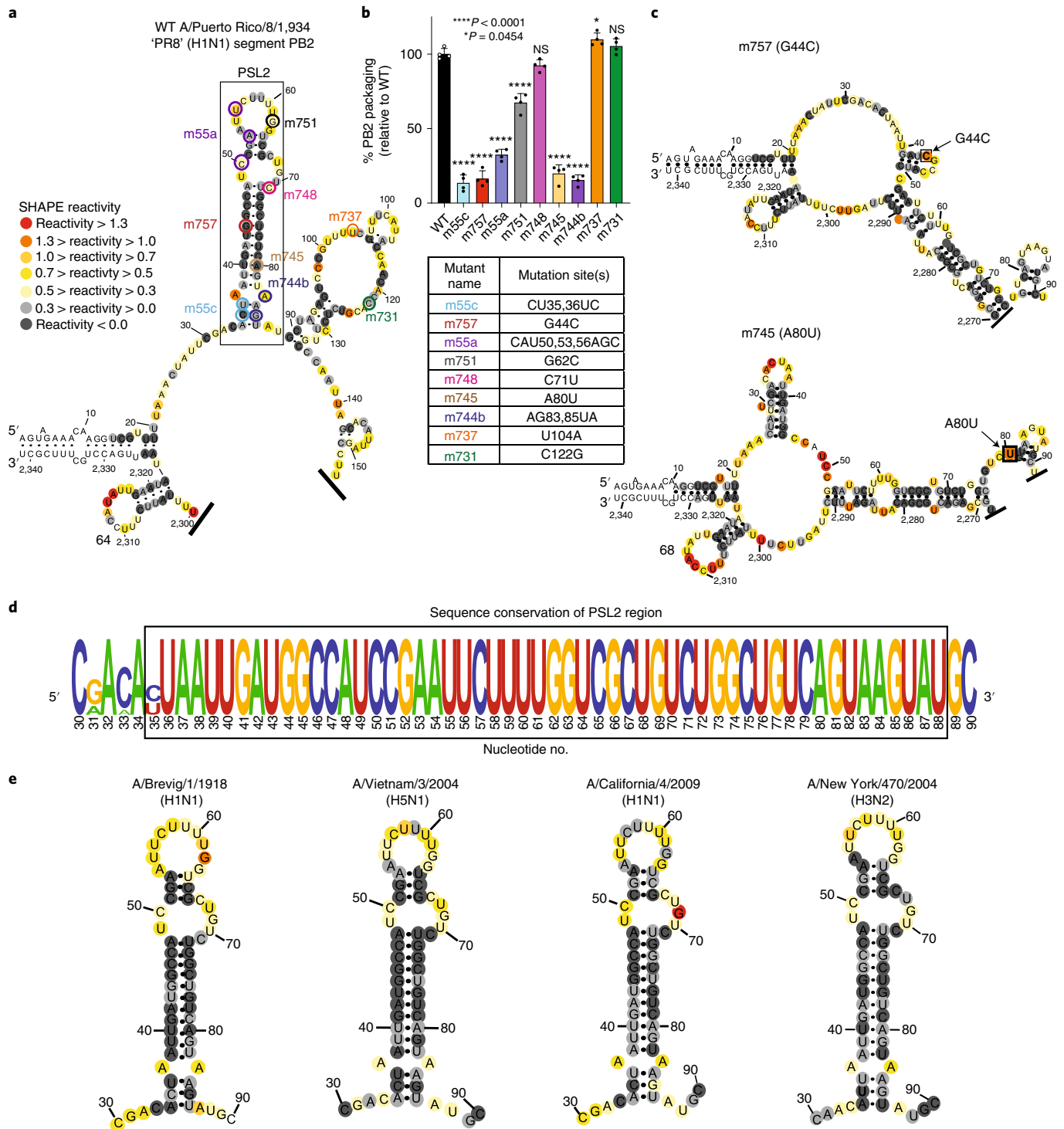
The IAV genome consists of eight single-stranded, negative-sense viral RNA (vRNA) segments that encode a minimum of 14 known viral proteins⁶. The vRNA, together with nucleoprotein (NP) and the heterotrimeric polymerase complex, comprising PB2, PB1 and PA proteins, forms the complete viral ribonucleoprotein (vRNP)⁷. To be fully infectious, IAV virions must incorporate at least one of each segment's vRNP⁸. The current paradigm supports a selective packaging method whereby the eight vRNPs are selected in a hierarchical manner mediated by unique, segment-specific packaging signals present in the terminal and central coding regions of each vRNA that allow for discrimination between the latter^{9–11}. Each vRNP interacts with at least one other partner vRNP to form a supramolecular complex¹² probably maintained by intersegment RNA–RNA and/or protein–RNA interactions hypothesized to guide the packaging process^{8,13}. The mechanism mediating this selection and arrangement is, however, poorly understood. Curiously,

¹Virx@Stanford, Stanford Medicine, Stanford, CA, USA. ²Department of Microbiology & Immunology, Stanford University School of Medicine, Stanford, CA, USA. ³Department of Medicine, Division of Gastroenterology and Hepatology, Stanford University School of Medicine, Stanford, CA, USA.

⁴Department of Biochemistry, Stanford University, Stanford, CA, USA. ⁵Department of Epidemiology, University of North Carolina at Chapel Hill, Chapel Hill, NC, USA.

⁶Division of Infectious Diseases and Geographic Medicine, Department of Medicine, Stanford University, Stanford, CA, USA. ⁷Institute for Antiviral Research, Department of Animal, Dairy, and Veterinary Sciences, Utah State University, Logan, UT, USA. ⁸Department of Medicine, Biomedical Informatics Research, Stanford University School of Medicine, Stanford, CA, USA. ⁹Department of Internal Medicine, Division of Infectious Diseases, University of Cincinnati College of Medicine, Cincinnati, OH, USA.

¹⁰Department of Microbiology and Immunology, University of Texas Medical Branch, Galveston, TX, USA. ¹¹Center for Biodefense and Emerging Diseases, Galveston National Laboratory, University of Texas Medical Branch, Galveston, TX, USA. ¹²Viral Pathogenesis and Evolution Section, Laboratory of Infectious Diseases, National Institute of Allergy and Infectious Diseases, National Institutes of Health, Bethesda, MD, USA. ¹³Chan Zuckerberg Biohub, San Francisco, CA, USA. ¹⁴Department of Physics, Stanford University, Stanford, CA, USA. ¹⁵Veterans Administration Medical Center, Palo Alto, CA, USA. ✉e-mail: jeffrey.glenn@stanford.edu



packaging signals exist in regions of high nucleotide conservancy that strongly suppress synonymous codon usage^{14–16}. Conservation of the primary sequence beyond what is required for protein coding suggests the potential for maintenance of RNA structures possessing biological functionalities. Certain synonymous mutations within the polymerase gene, *PB2*, affect not only its own packaging, but also the incorporation of other segments^{11,14,17}.

We hypothesized that *PB2*'s dominant role in the packaging process might be facilitated by nonprotein elements encoded by the *PB2* vRNA, including structured RNA elements. To test this hypothesis, we first mapped the RNA secondary structure within *PB2* that

mediates packaging, and then genetically validated this structure's role in the viral lifecycle in vitro and IAV pathogenesis in vivo. With this model, we demonstrate proof of concept for a new class of anti-viral therapeutics that can efficiently disrupt packaging and prevent and treat otherwise lethal IAV disease in vivo, as well as enable the development of strong functional immunity in mice, with a high barrier to resistance. Moreover, we hypothesized that an analogous approach can be applied to any RNA virus of interest, and the recent coronavirus (COVID-19) pandemic provided an opportunity for us to successfully test this hypothesis by targeting severe acute respiratory syndrome coronavirus 2 (SARS-CoV-2) in vitro and in vivo.

Fig. 1 | SHAPE-determined RNA secondary structures of WT PB2 and packaging mutant vRNAs. SHAPE-chemical mapping was performed on full-length (–)-sense PB2 vRNAs. Colors denote SHAPE reactivity, which is proportional to the probability that a nucleotide is single stranded. All structures are truncated to highlight the 5′-terminal sequence structure. **a**, SHAPE-predicted WT PB2 RNA secondary structure from strain A/Puerto Rico/8/1934 ‘PR8’ (H1N1). Color-coded circles correspond to nucleotide sites where synonymous mutations were reported to affect PB2 packaging^{11,14}. **b**, Packaging efficiency of synonymous mutants in **a**, determined by RT-qPCR. Results represent two independent experiments with biological replicates, each performed in triplicate. Statistical analysis was performed using one-way ANOVA with Dunnett’s multiple comparison test against the WT mean by GraphPad Prism 9 software ($n = 4$). Error bars represent mean \pm s.d. **** $P < 0.0001$; * $P = 0.0454$; NS, not significant. The box below indicates mutant name and corresponding nucleotide change. Nucleotide numbering is shown in the genomic (–)-sense orientation. **c**, SHAPE-mapped structures of PB2 packaging-defective mutant vRNAs, m757 (G44C) and m745 (A80U) indicating loss of PSL2’s RNA secondary structure. The black arrowheads and boxed nucleotides denote site(s) of synonymous mutation. **d**, Web-logo representation of the PSL2 region conservation across IAV strains and diverse IAV subtypes (weblogo.berkeley.edu). The overall height represents sequence conservation at that nucleotide position, whereas the symbol height within each position indicates the relative frequency of each nucleotide at that site. The black box denotes the PSL2 region. Sequences included in the alignment are: pandemic A/Brevig Mission/1/1918 (H1N1), pandemic A/California/04/2009 (H1N1), seasonal human A/New York/470/2004 (H3N2), A/Puerto Rico/8/1934 (H1N1), highly pathogenic avian A/Vietnam/03/2004 (H5N1), avian A/mallard/Maryland/14OS1154/2014 (H6N1), pandemic A/Hong Kong/8/1968 (H3N2) and seasonal human A/New York/312/2001 (H1N1) (Supplementary Fig. 1d). RNA nucleotides are numbered in (–)-sense orientation. **e**, SHAPE-mapped structures of full-length WT PB2 vRNA from pandemic and highly pathogenic strains, including different subtypes to modern human strains: 1918 pandemic (A/Brevig Mission/1/1918 (H1N1)), highly pathogenic avian (A/Vietnam/1203/2004 (H5N1)), 2009 pandemic ‘swine’ (A/California/04/2009 (H1N1)) and Fujian-like human seasonal virus, A/New York/470/2004 (H3N2).

Results

SHAPE identifies conserved candidate PB2 packaging signal.

To search for structured RNA domains in IAV segments, we first applied selective 2′-hydroxylacylation analyzed by primer extension (SHAPE)¹⁸ and computational modeling to IAV segment PB2 genomic vRNA. In vitro transcribed, full-length (–)-sense PB2 vRNA from strain A/Puerto Rico/8/1934 (H1N1) PR8 was folded in solution¹⁹ and interrogated using an electrophilic SHAPE reagent that preferentially reacts with nucleotides existing in flexible, single-stranded states¹⁸ (Fig. 1). This analysis revealed that much of the 2,341-nucleotide (nt) vRNA is largely unstructured (Supplementary Fig. 1a), as described in previous genome analyses^{15,20}. However, these previous studies did not analyze the last 80 nucleotides of PB2’s terminal coding regions. SHAPE-guided modeling suggested several areas in this terminal region that contain stable RNA secondary structures, most notably a stem–loop motif, named herein as PSL2 (Fig. 1a and Supplementary Fig. 1b; nucleotides 34–87). This region includes a set of nucleotides that were previously implicated in segment PB2 packaging through mutational analysis via an unidentified mechanism (Fig. 1a,b, see circled nucleotides, and Supplementary Table 1)^{11,14,16}. Supporting the hypothesis that these prior mutations act through disruption of PSL2 structure, SHAPE analysis of the mutants yielded different conformations that all abrogated the wild-type (WT) PSL2 structure (Fig. 1c and Supplementary Fig. 2). The 60-nt region encompassing PSL2 displays almost 100% sequence conservation at the single-nucleotide level between representative seasonal and pandemic IAV strains of

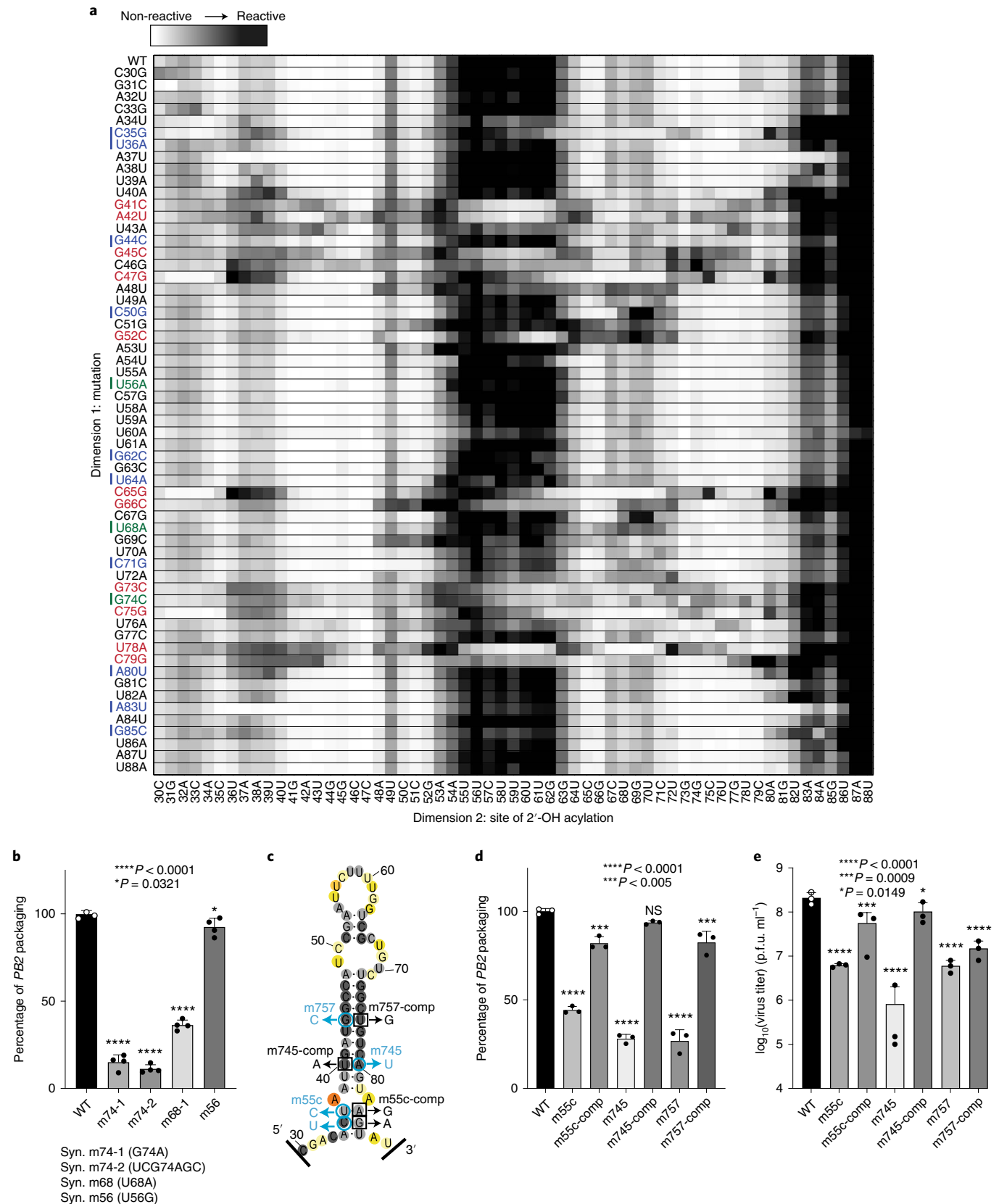
different subtypes and species origins (Fig. 1d and Supplementary Fig. 1c). Further analysis revealed that this high degree of conservation extends to all known IAV isolates available in public databases (Supplementary Fig. 1d), suggesting the existence of a strict biological requirement to maintain an intact PSL2 structure. Indeed, the PSL2 stem–loop structure was recovered in SHAPE-guided modeling of full-length PB2 RNA across diverse species and subtypes, including the highly pathogenic avian H5N1 and pandemic 1918 H1N1 strains (Fig. 1e).

M² validates PSL2 and predicts new packaging mutants. To further test the SHAPE analysis of the PSL2 RNA structure and to uncover additional informative mutations needed for in vivo tests, we applied multidimensional chemical-mapping methods to the PSL2 segment. Mutate-and-map (M²) analysis couples systematic mutagenesis with high-throughput chemical mapping to produce accurate basepair inferences and interactions of RNA domains²¹. By sequentially mutating RNA one nucleotide at a time with its Watson–Crick complement and measuring the impact that this mutagenesis has on chemical reactivity, pair-wise correlations between close and distant residues can be established. First, M² measurements confirmed disruption of the chemical reactivity pattern on systematic mutation of each PSL2 stem residue, including changes at nucleotides previously identified to be relevant for PB2 packaging (Fig. 2; see noted fields)^{11,14}. Automated computational analysis based on these M² data recovered the SHAPE-guided PSL2 structure with high confidence (Fig. 2 and Supplementary Fig. 3),

Fig. 2 | Two-dimensional M² analysis and empirical validation of the PSL2 motif. **a**, Systematic single-nucleotide mutation and mapping of resulting chemical accessibility reveals interactions in the three-dimensional structure of the RNA. Chemical accessibilities are plotted in gray scale (black, highest SHAPE reactivity), across 59 single mutations at single-nucleotide resolutions of PSL2 element from PR8 strain segment PB2. Reactivity peaks (left to right) correspond to nucleotides from the 5′- to the 3′-end of the PB2 RNA. Nucleotides corresponding to known packaging mutation sites¹¹ are indicated on the left in blue. Red emboldened mutations denote packaging-defective mutant sites predicted by M² analysis. Green emboldened mutations indicate synonymous mutant sites analyzed in **b**. **b**, Packaging efficiencies of M²-identified synonymous mutants readout by RT-qPCR. Packaging efficiency represents the percentage of mutant PB2 vRNA packaging relative to parental WT PB2. The results are from two independent experiments in biological duplicate and technical triplicate ($n = 4$). **** $P < 0.0001$, * $P = 0.0321$. **c**, Previously described synonymous (Syn.) mutants (m757, m745, m55c) are mapped on to the PSL2 structure. Compensatory, nonsynonymous mutations m55c-comp, m745-comp and m757-comp were designed at sites predicted to restore WT PSL2 structure based on SHAPE and M² chemical analyses. Black boxed nucleotides denote compensatory mutation sites. The (–)-sense vRNA orientation is shown. **d**, Packaging efficiencies of packaging-defective and compensatory mutant viruses. For compensatory mutations where a nonsynonymous change was required, a WT PB2 protein expression plasmid was co-transfected during virus rescue. Values are given as percentage of PB2 vRNA packaging relative to WT PR8 virus. The results are from three independent experiments ($n = 3$), with assays performed in triplicate. **** $P < 0.0001$, *** $P < 0.0005$; NS, not significant. **e**, Virus titer determined by plaque assay. Results are expressed in p.f.u. ml⁻¹, with plaque assays in triplicate ($n = 3$). **** $P < 0.0001$, *** $P = 0.0009$, ** $P = 0.0149$. All error bars represent mean \pm s.d. All statistical analyses were performed by ordinary one-way ANOVA using Dunnett’s multiple comparison test against WT computed in GraphPad Prism 9 software.

further validating our structural model. Second, as predictive tests, we designed compensatory mutations to restore basepairings—albeit not the native sequence—in the WT structure that were disrupted by the initial packaging-defective mutations (Supplementary

Fig. 4). These mutation–rescue variants restored the PSL2 SHAPE pattern, providing *in vitro* validation of the modeled structure at basepair resolution and suggesting sequence variants to test the role of PSL2 structure *in vivo*.



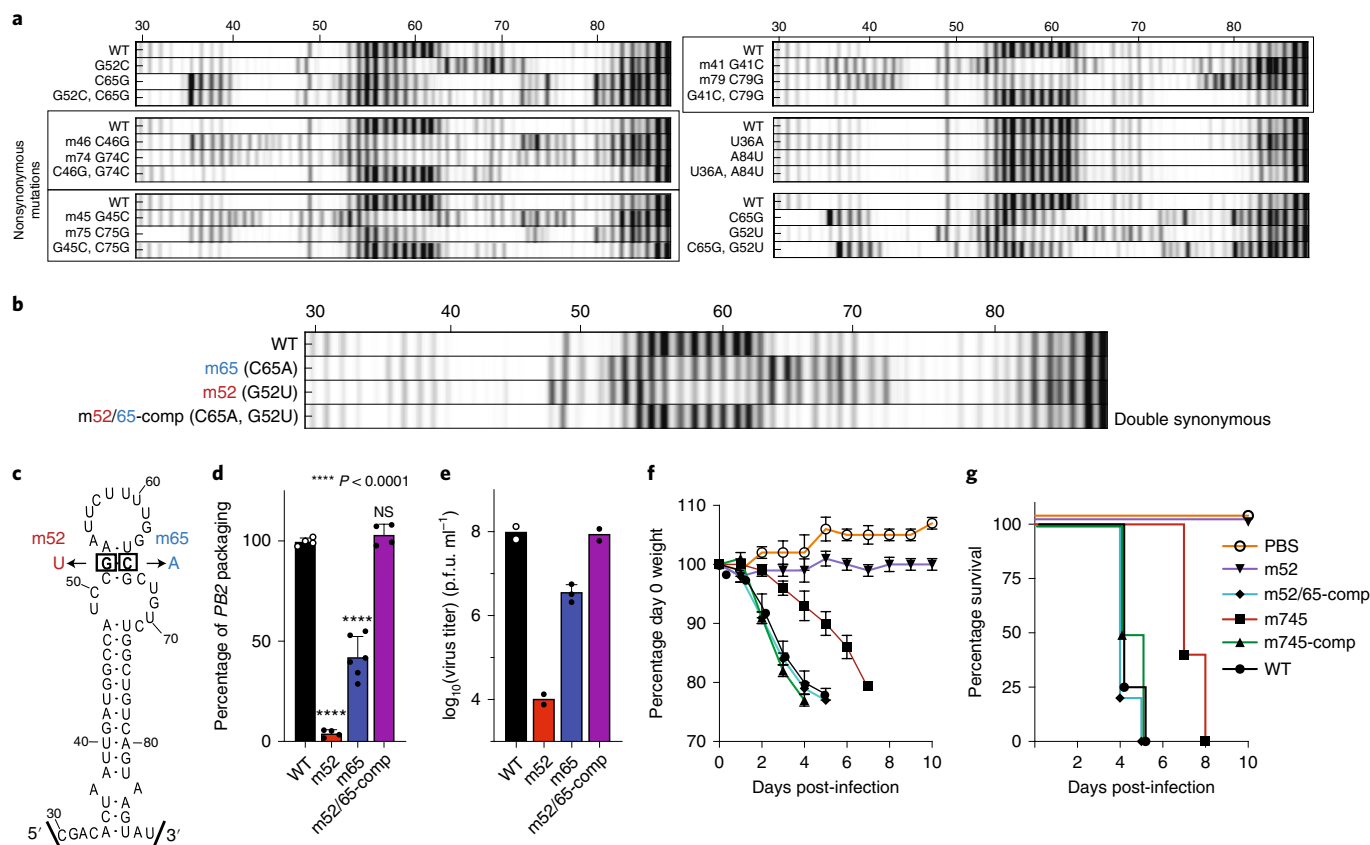


Fig. 3 | Mutate-map-rescue analysis reveals new PB2 packaging-defective and compensatory mutant partners. **a**, Electropherograms from systematic single-nucleotide mutation SHAPE chemical mapping with rescue (mutate-map-rescue)²¹ analysis of individual and compensatory double mutations to test basepairings from 1D data-guided models and to identify predicted successful synonymous PSL2-defective and compensatory mutant pairs. Chemical accessibilities are plotted in gray scale (black = highest SHAPE reactivity), across 59 single mutations at single-nucleotide resolutions of the PSL2 element from the PR8 strain segment PB2. Reactivity peaks (left to right) correspond to nucleotides from the 5'- to the 3'-end of the PB2 RNA (see Supplementary Fig. 7 for a complete set of M²R pairs). **b**, Electropherogram of successful double synonymous mutant pair determined by the mutate-map-rescue analysis. **c**, Mutational design of single mutants m52 (G52U) and m65 (C65A), and the double m52/65-comp rescue pair on the PSL2 structure. **d**, Packaging efficiency of the synonymous single and double-mutant M²R pair. Values are given as a percentage of PB2 vRNA packaging relative to WT PR8 virus. Results represent two independent experiments with biological duplicates performed in technical triplicate ($n = 4$), except for m65 performed in biological triplicate ($n = 6$). Statistical analysis is by ordinary one-way ANOVA using Dunnett's multiple comparison test against WT. * $P < 0.0001$; NS, not significant. **e**, Viral titer of the supernatants collected in **d** in p.f.u. ml⁻¹, plaque assays in biological duplicate ($n = 2$), except for m65 ($n = 3$), and performed in technical triplicate. **f, g**, Percentage of day 0 weight and survival of mice infected with single PSL2-disrupting and compensatory PSL2-restoring double-mutant viruses; 6- to 8-week-old female BALB/c mice ($n = 6$) were intranasally infected with PR8 WT virus, packaging-defective single mutant viruses, m52 and m745, compensatory double-mutant viruses, m52/65-comp and m745-comp, or PBS control. **f**, Percentage of day 0 weight. **g**, Kaplan-Meier survival plot of the individual cohorts depicted in **f**. All error bars represent mean \pm s.d. Statistics and graphs for all figures were generated in GraphPad Prism 9 software.

To test whether the PSL2 stem-loop structure observed in solution was relevant to virus packaging in the cellular milieu, the same nine synonymous mutations reported by Gog et al. and Marsh et al. (Fig. 1a,b and Supplementary Table 1), as well as four new synonymous mutations characterized by M² analysis (Fig. 2a,b), were cloned into plasmids containing the PR8 PB2 gene^{11,14,16}. The packaging efficiencies of the nine previously known mutants, now in the PR8 background, were comparable to those originally described in the WSN33 virus¹¹ (Fig. 1b and Supplementary Table 1). Of these, mutants m55c, m757, m745 and m744b were predicted to show the most notable impairment based on their location within PSL2's stem regions (Fig. 1a-c and Supplementary Fig. 2). In contrast, published mutations that have no effect on PB2 packaging (for example, m731) mapped to the unstructured apical loop or fell outside of PSL2 and did not alter its structural integrity (Supplementary Fig. 5a), whereas mutations with minor effects on virus packaging

showed only minor alterations to the structure (Supplementary Fig. 5b)¹¹. The three new synonymous mutants (m74-1, m74-2 and m68) identified by M² analysis as having a substantial effect on in vitro PSL2 structure (Fig. 2a, see green-marked nucleotides) showed significant loss in PB2 WT-like packaging efficiency levels (Fig. 2b). The strong correlation of structure disruption with in cellulo packaging efficiency observed across these mutants supports a role of PSL2 structure in virus packaging.

Compensatory mutations restore PSL2 structure and function.

To investigate the functional role of PSL2 in IAV genome packaging, compensatory mutations designed to restore the WT stem-loop structure destroyed by the packaging-defective mutations (Fig. 2c and Supplementary Fig. 4) were cloned into PR8 expression plasmids to generate mutant rescue viruses. The compensatory mutations rescued not only the virus packaging for segment PB2

(Fig. 2d), but also other segments previously reported to be affected by the deleterious mutations, consistent with the proposed hierarchical role of *PB2* in IAV packaging (Supplementary Fig. 6a)^{10,11,17}. In addition to recovering *PB2* packaging, the compensatory mutations gave complete or near-complete rescue of the virus titer loss caused by the defective mutations (Fig. 2e and Supplementary Fig. 6b). Some nonsynonymous compensatory mutations were able to restore *PB2* packaging better than others (for example, m745-comp compared with m757-comp). This possibly reflects incomplete restoration of *PB2* protein function through exogenous addition (Fig. 2d,e and Supplementary Fig. 6) because, for nonsynonymous mutations, we also expressed WT *PB2* protein to mitigate the possibility of any impairment in *PB2* protein function.

We performed computational enumeration and multidimensional mutation–rescue²² (M²R) experiments to identify additional successful PSL2-defective and compensatory mutant pairs (Fig. 3a,b and Supplementary Fig. 7). Successful M²R was defined when each single mutation alone disrupted the SHAPE-mapped WT PSL2 structure, while the double compensatory mutations recovered its structure (Fig. 3a,b, see boxed electropherograms). Although most successful partners required nonsynonymous changes, we discovered a single M²R pair of synonymous substitutions that obviated WT *PB2* protein addition (Fig. 3b,c and Supplementary Fig. 7). Making each mutation alone (m52 and m65) resulted in severe packaging defects and, in the case of the m52 mutation, virus titer loss exceeding 4log₁₀—an extreme impairment beyond the 1–2log₁₀ that had been previously reported^{11,14} for packaging-defective viruses (Fig. 3d,e and Supplementary Figs. 6 and 8). When introduced together into a doubly mutated m52/65-compensatory virus that restored PSL2 structure, albeit with an altered sequence, the compensatory mutations restored both packaging efficiency and virus titer to WT levels.

To ensure that any loss or subsequent rescue of virus production caused by these mutations was not due to defects in replication or translation, each M²R pair was tested in transfection-based replicon assays. All mutant *PB2* proteins and vRNAs were produced at comparable WT levels (Supplementary Figs. 9 and 10). As an orthogonal means of testing packaging efficiency, we also assessed the effect of select mutations on vRNA packaging by denaturing RNA gel, which recapitulated our earlier packaging findings (Supplementary Fig. 11c, Figs. 2d and 3d, and Supplementary Fig. 6).

To test the relevance of the PSL2 structure in an in vivo model, BALB/c mice were intranasally infected with either WT or mutant PR8 viruses harboring point mutations predicted to disrupt or restore PSL2 structure. Mice infected with the PSL2-disrupting mutations—m745 mutant strain (20% packaging efficiency) or the severely defective mutant virus, m52 (<4% packaging efficiency)—showed reduced or no clinical signs of illness, respectively, either in weight loss or in survival compared with the phosphate-buffered saline (PBS) control (Fig. 3f,g). In contrast, inclusion of

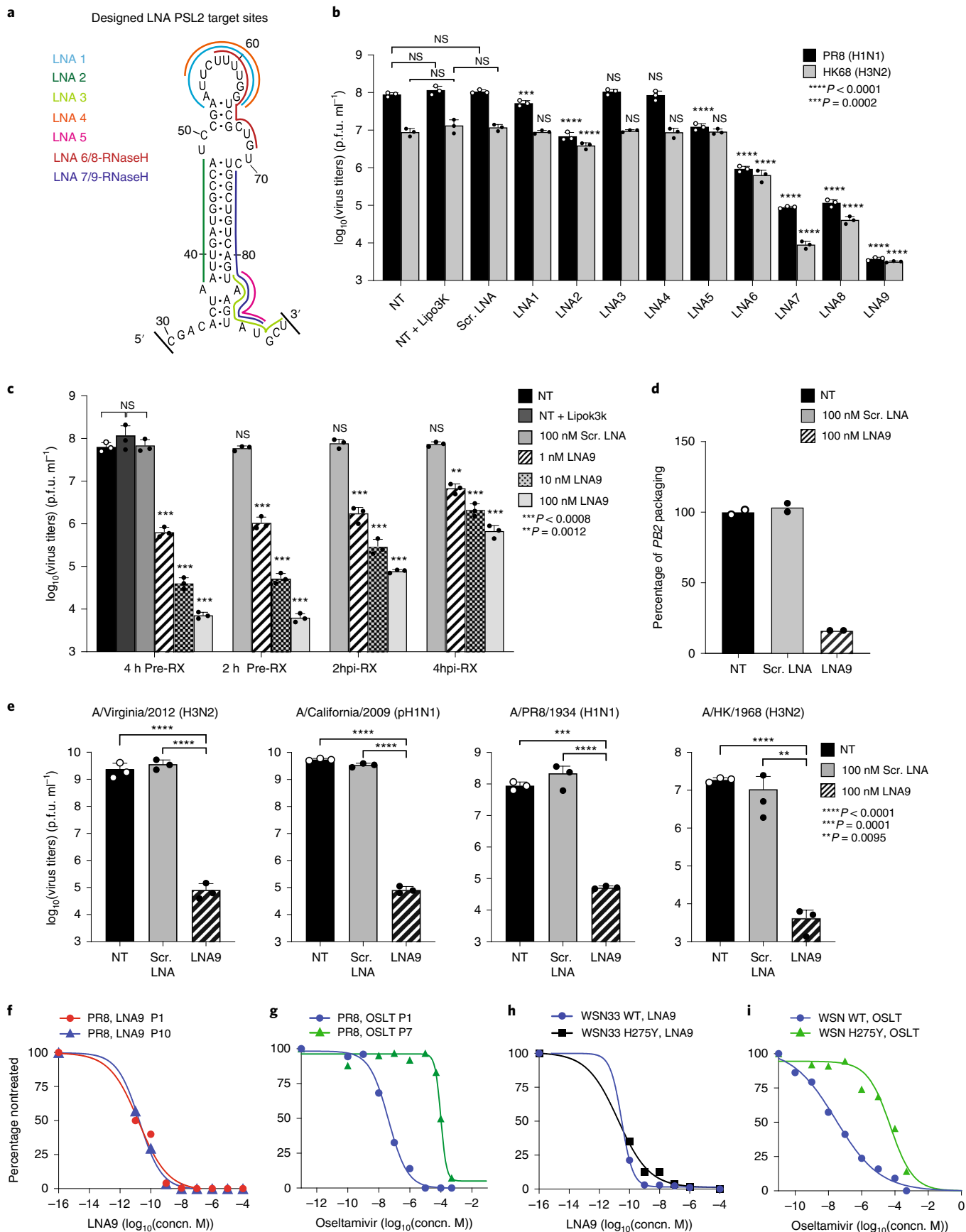
compensatory mutations that restore the PSL2 structure rescued virus pathogenicity: animals infected with m52/65-comp and m745-comp displayed comparable mortality profiles to mice infected with WT PR8 (Fig. 3f,g). To the best of our knowledge, these are probably among the first data to indicate that packaging-defective viruses are attenuated in vivo and a genomic IAV RNA secondary structure mediates influenza disease progression.

Designing anti-IAV LNA therapeutics targeting the PSL2 structure. Given the strong evolutionary conservation of the PSL2 structure (Fig. 1d,e and Supplementary Fig. 1c,d), we postulated that PSL2-targeted therapeutics could possess broad-spectrum activity across IAV subtypes and strains. Nine antisense oligonucleotides (ASOs) with modified LNA bases²³ were designed against PSL2 to disrupt various regions of the overall RNA secondary structure (Fig. 4a). Two LNAs, LNA8 and LNA9, are identical in sequence to LNA6 and LNA7, respectively, but possess six or seven unmodified (nonlocked) DNA nucleotide ‘gapmers’ optimized for RNase-H activation that can degrade RNA in RNA–DNA hybrids²⁴. First, to assess the impact that LNA binding has on PSL2 RNA secondary structure, toeprinting and SHAPE chemical mapping were performed on *PB2* vRNA in the presence of the LNAs. Sequences encoded in LNA6–LNA9, corresponding to binding sites on the right 3′-side of the stem–loop structure (Fig. 4a), exhibited the greatest ability to bind and disrupt the WT PSL2 structure (Supplementary Fig. 12).

To test LNA-mediated targeting of PSL2 across different viral subtypes, Madin–Darby canine kidney (MDCK) cells were treated with LNA before infection with either PR8 (H1N1) virus or the tissue-culture-adapted A/Hong Kong/8/1968 (HK68) (H3N2) virus, and virus inhibition was assessed by plaque assay (Fig. 4b). As predicted by the mutational and LNA chemical-mapping experiments (Fig. 2 and Supplementary Fig. 12), LNAs directed against only the top loop of PSL2 (LNA1, LNA4), and LNAs solely targeting the 3′-base of PSL2 (for example, LNA3 and LNA5) had minimal effect on viral titer. In contrast, nucleotide coverage of both the top loop and the middle bulge by LNA6 resulted in >2log₁₀ titer deficits for PR8 (Fig. 4a,b). LNA8, the RNase-H-activated copy of LNA6, produced even greater antiviral activity against both viruses of up to 3log₁₀. Notably, LNA9, the RNase-H-activated copy of LNA7, possessed the strongest antiviral capacity, inhibiting virus production by over 4log₁₀ and 3log₁₀ against PR8 and HK68, respectively. Although a labeled version of LNA9 could be clearly visualized in cells harboring vRNPs (Supplementary Fig. 13), no off-target effect of LNA9 on steady-state levels of viral protein, vRNA, complementary RNA or cellular toxicity after 24 h was observed (Supplementary Fig. 14).

Having identified a potent candidate LNA, we next investigated the treatment time-course and concentration parameters of LNA9’s antiviral activity when administered prophylactically at 2 and 4 h pre-infection, and therapeutically at 2 and 4 h post-infection. Cells pretreated with the LNA had the most potent antiviral

Fig. 4 | LNAs targeting PSL2 RNA structure display potent antiviral activity in vitro. **a**, Regions of PSL2 targeted by indicated LNAs. **b**, Antiviral screen of LNAs transfected into MDCK cells and infected 4 h later with PR8 (H1N1) or A/Hong Kong/8/68 (H3N2) virus (0.01 MOI) and viral titers determined 48 h post-infection ($n=3$). Statistics performed by unpaired, ordinary one-way ANOVA (PR8 and HK68) with Dunnett’s multiple comparison test. **c**, Antiviral efficacy as a function of time of LNA addition ($n=3$), analyzed as in **b**. Statistics are by two-way ANOVA with Dunnett’s multiple comparison test against nontreated +Lipo3k (NT). **d**, *PB2* vRNA (PR8) packaging efficiency of viruses treated with 100 nM LNA9 or Scr. LNA control. Values are given as a percentage of *PB2* vRNA packaging in comparison to NT WT PR8 virus; readout by qPCR. The results are from two biological replicates ($n=2$), assays performed in technical triplicates. **e**, LNA9 efficacy against multiple IAV strains in MDCK cells pretreated with 100 nM of indicated LNAs, analyzed as in **b**. The statistics are as described in **c** against the NT control. **f**, In vitro selection for drug resistance to LNA9 with escalating concentrations of LNA and the sensitivity of passaged virus in response to drug treatment. The EC₅₀ values are determined at the indicated passage (P) numbers. The results are expressed as a percentage of NT virus titer. **g**, In vitro selection of PR8 virus selected with OSLT. OSLT-treated PR8 virus and drug sensitivity were determined by plaque reduction assay. The number of viral plaques with each drug concentration was normalized against the NT control to determine the EC₅₀. **h**, In vitro sensitivity of WT WSN33 (H1N1) and NAI-resistant (WSN H275Y NA mutant) virus to LNA9 (**h**) or OSLT (**i**). The EC₅₀ values were computed using a nonlinear regression model with variable slope. Statistics for all graphs performed in GraphPad Prism 9 software. All error bars represent mean ± s.d. *Statistical P value is indicated in each panel.



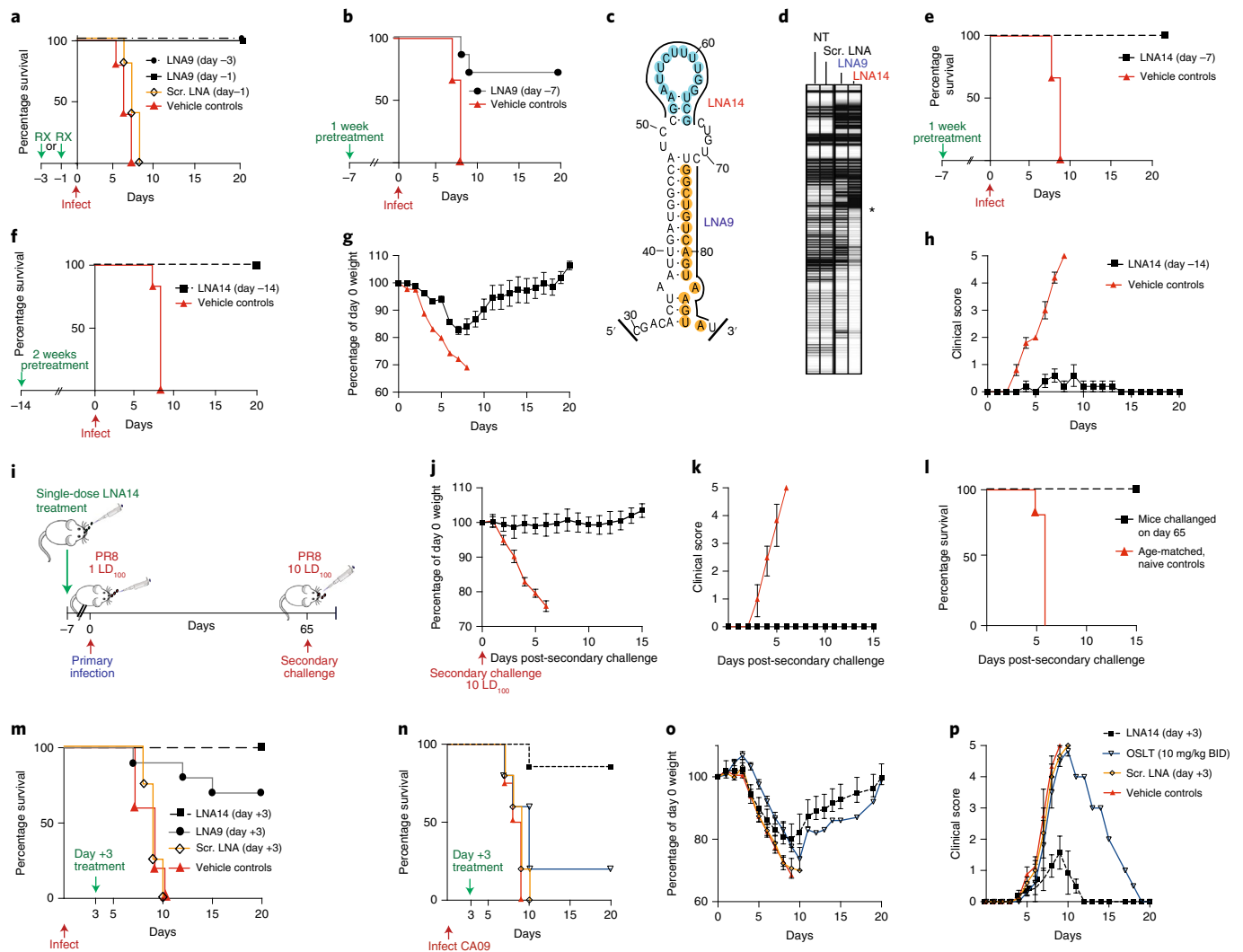


Fig. 5 | PSL2-targeted LNAs demonstrate potent antiviral activity in vivo. **a,b**, Kaplan–Meier survival plots of mice intranasally administered a single dose of LNA9, Scr. LNA or vehicle (mock treated) on the indicated days with respect to a subsequent lethal inoculum of WT PR8 virus (PR8): 20 μ g of LNA9 ($n=5$) (**a**), 30 μ g of LNA9 ($n=7$) (**b**) or vehicle control ($n=5$). **c**, Target sites of LNA9 and newly designed LNA14, mapped to the PSL2 structure. **d**, Electrophoretic profile of SHAPE analysis performed on PR8 PB2 vRNA in the presence of nontreated or 100 nM Scr. LNA, LNA9 or LNA14. The asterisk marks the site of RT stops, indicating the strength of LNA–RNA binding. **e,f**, Kaplan–Meier survival plots of mice pretreated with a single intranasal dose of 30 μ g of LNA14 ($n=7$) or vehicle ($n=5$), day -7 (**e**), 40 μ g of LNA14 or vehicle ($n=6$), day -14 (**f**), before receiving lethal PR8 inoculum. **g,h**, Percentage of day 0 weights (**g**) and clinical score (**h**), of mice from **f**. Error bars show mean \pm s.e.m. **i–l**, Mice ($n=7$) from **e**, who had received a single 30- μ g intranasal dose of LNA14 1 week before a first lethal inoculum (1 LD₁₀₀) of PR8 that all survived, inoculated 65 d post-initial infection, along with age-matched naive controls ($n=10$), with 10 LD₁₀₀: challenge study timeline (**i**); weight loss (**j**); clinical score (**k**); and Kaplan–Meier survival curve (**l**). Error bars show mean \pm s.d. **m**, Kaplan–Meier survival plot of mice ($n=10$ per group) infected with a lethal dose of PR8, followed 3 d later with a single intravenous dose of 30 μ g of LNA14, LNA9, Scr. LNA or vehicle control. **n–p**, Mice infected with a lethal dose of mouse-adapted A/California/04/2009 (pH1N1) virus (CA09), then treated intranasally with a single 30- μ g dose of LNA14 ($n=7$ per group), Scr. LNA ($n=5$) or vehicle ($n=4$) on day +3 post-infection. Mice given OSLT ($n=5$) were treated by oral gavage twice daily for 5 d starting at day +3: Kaplan–Meier survival curve (**n**); percentage of day 0 weight (**o**); and clinical score (**p**). All studies were performed with 6- to 8-week-old female BALB/c mice. Error bars in **o** and **p** indicate mean \pm s.e.m.

response ($<4\log_{10}$) and displayed strong virus inhibition even at the lowest concentration tested (1 nM) (Fig. 4c). There was a trend toward decreasing antiviral activity as the time of administration post-infection increased, but, even at the latest tested time point of addition, $>2\log_{10}$ suppression of viral titer was achieved. Similar efficacy was seen in the presence of a high multiplicity of infection (MOI) (Supplementary Fig. 15). Furthermore, LNA9 treatment resulted in a dramatic loss of PB2 packaging compared with controls (Fig. 4d), an effect that resembled the mutational studies and extended to the 2009 pandemic virus (pH1N1) and 2012 H3N2 virus, indicating the potential for broad-spectrum antiviral activity.

Selection of IAV variants with escalating drug pressure. To test the hypothesis that the high conservation of PSL2 reflects a biological constraint against mutation of this structure, and that this could translate into a high barrier to the development of resistance for PSL2-targeting therapeutics, we determined the susceptibility of WT PR8 virus to LNA9 under conditions designed to promote the development of resistance over serial virus passaging (Fig. 4f). In parallel, we performed analogous experiments using the neuraminidase inhibitor (NAI) oseltamivir carboxylate (OSLI, Tamiflu). After seven virus passages in the presence of escalating drug concentrations, the half-maximal effective concentration (EC₅₀) of

OSLT increased from 4.1 nM to 100 μ M—a >20,000-fold increase (Fig. 4g). In comparison, after ten virus passages in the presence of LNA9, the EC₅₀ value showed no significant change and remained in the range 16–22 pM (Fig. 4f). To date, we still have been unable to select for viral mutations capable of generating resistance to LNA9. Moreover, LNA9 was equally effective (EC₅₀ = 18 pM) against a virus strain (A/WSN/33 (H1N1)) containing the H275Y mutation (N1 numbering system) that confers resistance to OSLT, whereas high-level resistance to OSLT was confirmed, with an EC₅₀ of 53 μ M (Fig. 4h,i). These results extend the therapeutic capabilities of LNA9 and provide strong support for potential treatment of NAI-resistant viruses with PSL2-targeting LNAs.

PSL2-targeted LNAs protect mice from lethal IAV infections. As a proof of concept to assess the in vivo efficacy of prophylactic LNA treatment against PSL2, BALB/c mice were intranasally administered a single 20- μ g dose of LNA9 or scrambled (Scr.) LNA 1 or 3 d before infection with a lethal dose of PR8 virus. The untreated control mice experienced dramatic weight loss and were humanely sacrificed by days 5 and 6. In contrast, a single intranasal dose of LNA9 was completely protective when administered 1 d, and even 3 d, before viral infection (Fig. 5a) and showed significantly reduced virus titers in the lungs (>2.5log₁₀ virus reduction) compared with the Scr. LNA control at 72 h post-infection (Supplementary Fig. 16). In addition to the well-known benefits of LNA antisense gapmer technology that enables recruitment of RNase-H to degrade the targeted RNA^{23,24}, LNA ASOs have also been reported to show dramatic, long-lasting effects (even >1 month) after the last administered dose in a variety of disease models^{25–28}. We hypothesized that PSL2-targeted LNAs might similarly possess long-term prophylactic effects due to the nuclease-resistant property conferred by the phosphorothioate backbone present in LNAs.

To test this hypothesis, we administered a single, increased dose of LNA9 (30 μ g) 1 week (day –7) before infection with a lethal dose of IAV. Although 100% of untreated mice succumbed to the infection, 70% of the LNA9 1-week pretreatment group were protected from lethality (Fig. 5b). To determine whether our therapeutics could be further optimized for improved efficacy, we explored targeting other sequences in PSL2. Although LNA9 targets nucleotides in the lower 3'-stem of PSL2, our mutational analyses suggested the importance of the 52- to 65-nt pair in the upper stem (Fig. 3). We hypothesized that an LNA designed against these nucleotides (LNA14) might enhance efficacy (Fig. 4a). Indeed, SHAPE analysis indicated that LNA14 was an even more potent disruptor of PSL2 structure than LNA9 (Fig. 5c,d). In biological confirmation of this, mice treated with LNA14 were fully protected when given a single dose 1 week before infection with a lethal dose of IAV (Fig. 5e). When we increased the LNA dosage to 40 μ g and administered a single LNA14 treatment to mice 2 weeks (day –14) before

IAV infection, the mock-treated mice succumbed to infection between days 7 and 8 due to severe disease, whereas the entire LNA14-treated cohort survived, with significantly lower disease scores, indicative of minor-to-undetectable disease symptoms and reduced weight loss compared with controls (Fig. 5f–h and Supplementary Table 2).

We attribute the LNAs' antiviral effect to their direct binding of PSL2, as opposed to nonspecific activation of antiviral pathways. Indeed, LNA14, LNA9 or derivative molecules did not elicit activation of either interferon (IFN)-stimulated genes or the NF- κ B (nuclear factor κ -light-chain-enhancer of activated B cells) pathway in lung or myeloid cells (Supplementary Fig. 17).

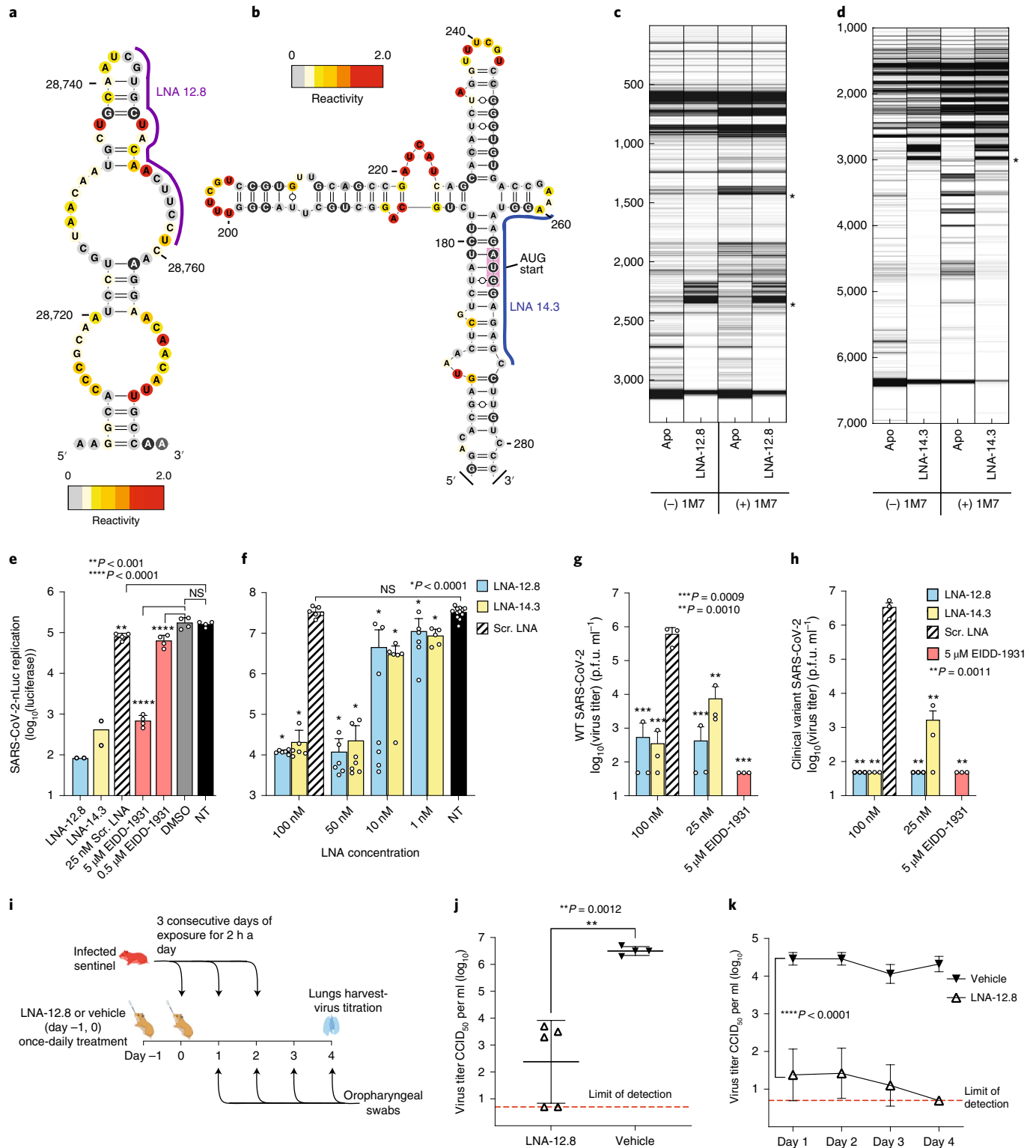
Given the mild symptoms observed in LNA-treated and -protected mice, we hypothesized that the resulting highly attenuated infection might be sufficient to enable mice receiving prophylactic LNA treatment to develop an effective immunization against a secondary infection through production of immunity. To test this hypothesis, mice from the 1-week LNA14 pretreatment-surviving cohort (Fig. 5e) were challenged alongside age-matched, naive controls, 65 d post-primary infection with ten times the mouse lethal dose (10 LD₁₀₀) of IAV (Fig. 5i). The secondary challenge had no effect on weight, clinical score or survival of mice from the LNA14 pretreatment group (a total of 72 d since treatment or 65 d since primary infection), whereas the age-matched controls presented with rapid disease and were humanely sacrificed by day 6 post-challenge infection (Fig. 5j–l). Blood and spleen cells were analyzed for the presence of virus-specific T cells and the development of antibodies against viral proteins (Supplementary Fig. 18a,b), which demonstrated stimulation of both the cellular and the humoral arms of the immune system, although their respective contributions to complete absence of symptoms after a tenfold higher lethal inoculum await definition.

After demonstrating PSL2-targeted LNA efficacy in prophylactic models, we next tested its potential as a post-infection therapeutic. Due to the rapid onset of symptoms and illness in IAV infections, US Food and Drug Administration-approved IAV therapeutics are most challenged when administered after 48 h of disease onset²⁹. In contrast, we hypothesized that anti-PSL2 LNAs, administered either intravenously or intranasally, could treat IAV well after an infection has been established. To test this hypothesis, mice infected with a lethal dose of PR8 virus were treated with LNA14, LNA9, Scr. LNA or vehicle control by intravenous injection 3 d post-infection (day +3) when mice typically become noticeably ill. Although animals treated with controls rapidly succumbed to the infection, 65% of mice treated with LNA9 survived lethal infection and all the LNA14-treated mice survived (Fig. 5m). Next, we tested the therapeutic efficacy of LNA14 via intranasal administration against the 2009 modern pandemic 'swine' virus (A/California/04/2009 pH1N1; CA09), which has since become a dominant seasonal

Fig. 6 | Antisense targeting of highly conserved RNA secondary structures in SARS-CoV-2. **a,b**, Two SHAPE reactivity-derived prediction of RNA secondary structures within (+)-sense SARS-CoV-2 vRNA and LNAs designed against these targets: nt 28,743–28,827, LNA-12.8 (**a**) and nt 258–276, LNA-14.3 (**b**). **c,d**, Electrophoretic profile of SHAPE analysis performed in the presence or absence of the corresponding LNAs. **e**, In vitro antiviral activity of 25 nM LNAs against SARS-CoV-2-Nluc virus in Huh-7 cells ($n=4$). The nucleoside analog, EIDD-1931, was included as a positive control at 5 μ M and 0.5 μ M. **f**, LNA dose-response against SARS-CoV-2-Nluc virus in ACE2-TMPRSS2-Huh-7.5 cells, in biological replicates ($n=6-7$ for all treatment groups, except for NT controls where $n=12$). **g,h**, Virus titers of supernatant collected from A549-hACE2 cells treated with LNA or EIDD-1931 followed by infection with either WT SARS-CoV-2 (**g**) or a patient-isolated clinical variant of SARS-CoV-2 containing multiple mutations in the spike protein region, including Asp614Gly, Glu484Lys and Asn501Tyr present in variants of concern ($n=3$) (**h**). Statistical analysis in **e**, **f**, **g** and **h** was performed using ordinary one-way ANOVA with Dunnett's multiple comparison tests between the controls as indicated. Error bars represent mean \pm s.d.; P values are as indicated. **i-k**, Prevention of SARS-CoV-2 transmission in Syrian hamsters: 10-week-old female Syrian hamsters were pretreated with either 100 μ g of LNA-12.8 ($n=5$) or vehicle ($n=4$) on day –1 and day 0 before exposure to SARS-CoV-2-infected sentinel hamsters for 2 h per day for 3 consecutive days. Four days after the initial exposure, lungs were harvested, and virus titers determined by CCID₅₀ in triplicate: experimental timeline (**i**); virus titer of SARS-CoV-2 in lungs (two-sided, unpaired Student's t -test) (**j**); and oropharyngeal swabs of LNA- or vehicle-treated hamsters (two-way ANOVA with multiple comparison tests against the vehicle controls) (**k**). The assay method detection limit is 0.7log₁₀(CCID₅₀). Error bars represent mean \pm s.d. The panel **i** was created with BioRender.com.

strain worldwide. Mice were infected with a lethal dose of CA09, then given a single intranasal dose of LNA14, Scr. LNA or vehicle control 3 d post-infection. OSLT was used as a therapeutic control and administered by oral gavage twice daily for 5 consecutive days starting at 3 d post-infection. The virus was 100% lethal against the Scr. LNA and vehicle control mice, and only 2/7 OSLT-treated mice were protected from lethal disease (Fig. 5n,o). In comparison, 6/7 mice in the LNA14-treated group were protected from

lethality and collectively had much lower clinical scores than the other cohorts (Fig. 5p). Sampling of lungs taken 2 d after LNA14 treatment of CA09-infected mice (that is, 5 d post-infection) showed significantly reduced virus titers ($>6\log_{10}$ virus reduction) compared with the controls (Supplementary Fig. 19). We also observed good dose proportionality in the lungs up to the highest dose tested to date (80 μg of LNA14) (Supplementary Fig. 20). Lowering the LNA14 dose down to 5 μg still resulted in full protection from death



(Supplementary Fig. 21), whereas Scr. LNA offered no more protection than vehicle control.

Programmable antivirals against SARS-CoV-2 RNA structures. We hypothesized that we could leverage our approach to targeting IAV and similarly design potent LNAs against SARS-CoV-2. Briefly, we first performed sequence alignments of the entire 30-kb positive-sense RNA genome of SARS-CoV-2 and related beta-coronaviruses to identify conserved sequence regions predicted to contain RNA secondary structures³⁰. We then focused on highly conserved nucleotide stretches of sufficient length to enable antisense nucleotide attack, and a high probability of structural stability to identify promising candidate antiviral targets. SHAPE yielded high-resolution RNA secondary structure maps of these regions and guided LNA design. Highly conserved targets included a stem-loop structure near the end of the SARS-CoV-2 genome (nt 28,743–28,792; Fig. 6a) and the structured domain spanning the terminal 5'-UTR into the ORF1-coding sequence (nt 258–276; Fig. 6b). LNAs were vetted for their ability to disrupt these structures by chemical mapping of the LNA–RNA interaction (Fig. 6c,d).

The LNAs were then screened against a SARS-CoV-2-Nluc reporter virus under Biosafety Level 3 (BSL-3) conditions (Fig. 6e). The nucleoside analog, EIDD-1931 (ref. 31), was included as a positive control, and Scr. LNA and dimethylsulfoxide (DMSO) treated and nontreated (NT) served as negative controls. Both LNAs against these target structures inhibited virus replication by as much as $3\log_{10}$, with the 25 nM LNA-12.8 outperforming the 5 μ M EIDD control by nearly $1\log_{10}$ (Fig. 6e). Next, an LNA dose–response experiment with expanded replicates was performed in Huh-7.5 cells that were modified to overexpress the human angiotensin-converting enzyme 2 (hACE2) and transmembrane protease, serine 2 (TMPRSS2) receptors to enable more efficient virus replication³² (Fig. 6f). Indeed, the viral replication signal was enhanced by nearly $2.5\log_{10}$ compared with Huh-7 cells in this system (Fig. 6e). Even at the higher virus burden, however, all tested LNA concentrations displayed statistically significant virus inhibition in a dose-dependent manner compared with the Scr. LNA controls and were nontoxic to the cells at concentrations $10\times$ higher than the highest dose assayed for antiviral activity (Supplementary Fig. 22a). We next tested our LNAs against the fully intact WT SARS-CoV-2 virus in a lung epithelial cell line expressing hACE2-A549 (Fig. 6g), which confirmed the previous Nluc virus results, whereby LNA treatment displayed $>3\log_{10}$ (virus inhibition) for both LNAs at 100 nM and LNA-12.8 at 25 nM, and were nontoxic to cells tested up to 1 μ M (Fig. 6h and Supplementary Fig. 22b).

We next pretreated hACE2-A549 cells with LNAs and then infected them with a new SARS-CoV-2 clinical isolate (SARS-CoV-2/human/USA/OH-UC-1/2020 ON642077) derived from a chronically infected cancer patient, whose sequence had evolved over a 7-month infection period (Fig. 6h). This clinical isolate harbors multiple mutations including Leu452Arg, Asp614Gly, Glu484Ala/Gln and Asn501Tyr in the spike protein receptor-binding domain shown to be involved in antibody escape, enhancement of virus replication and increased transmission found in variants of concern including alpha, beta, delta, mu and omicron³³ (<https://covid.cdc.gov/covid-data-tracker/#published-sars-cov-2-sequences>) (Supplementary Table 3). Despite numerous mutations throughout the viral spike protein-coding region and elsewhere in the genome, the LNAs retained their high levels of potency against this variant: both 100 nM treatments, as well as the 25 nM LNA-12.8 treatment, demonstrated complete virus inhibition to the experimental limit of detection, equaling a $5\log_{10}$ drop-in virus titer (Fig. 6h).

Given the high transmissibility of SARS-CoV-2, we sought to test the effectiveness of LNA treatment to prevent or mitigate SARS-CoV-2 transmission in a Syrian hamster model. In this system, hamsters were pretreated intranasally with a single 100 μ g dose

of our top SARS-CoV-2 LNA candidate, LNA-12.8, on 2 consecutive days, day –1 and day 0, before exposure to infected sentinel hamsters (Fig. 6i). Pretreated cohorts were repeatedly exposed to the infected sentinels for 2 h a day for 3 consecutive days. Daily oropharyngeal swabs were collected. Then 4 d post-initial exposure, lungs were collected and virus titers of LNA-12.8-treated versus vehicle-treated animals were compared (Fig. 6j). LNA-12.8 dramatically reduced viral titers by over $3\log_{10}$ compared with vehicle in exposed animals, with two hamsters containing no detectable virus in their lungs (Fig. 6j). As shown in Fig. 6k, viral titers in the oropharyngeal swabs showed parallel reductions in response to LNA treatment to the viral titer reductions observed in the lungs, with all hamsters showing undetectable oropharyngeal viral titers by day 4. Collectively, our identification, design and targeting of highly conserved RNA secondary structures in IAV and SARS-CoV-2, are proof-of-principle evidence toward a new model of rapid and effective antiviral development.

Discussion

We describe in the present study the discovery and characterization of an RNA stem-loop structure, PSL2, that serves as a packaging signal for genome segment PB2. PSL2 is conserved across all known influenza A isolates. Knowledge of PSL2's RNA secondary structure helps explain previously discovered packaging-defective mutations and enables rational design of more potentially disrupting mutations. Compensatory mutations that restore PSL2's structure (but not primary sequence) rescue virus packaging and titer loss in vitro and restore lethality in vivo, thus providing strong genetic validation of PSL2's importance in influenza biology and disease. LNAs designed to disrupt PSL2 structure dramatically inhibit IAV in vitro against viruses of different strains and subtypes. In contrast to NAIs, such as OSLT, and the endonuclease inhibitor, baloxavir marboxil (Xofluza), which are vulnerable to drug-resistant mutations^{34–36}, our PSL2-targeting LNAs exhibit a high barrier to the development of resistance and are equally effective against WT and NAI-resistant viruses. In vivo, intranasal dosing of LNAs results in potent antiviral efficacy and prevents mortality in mice, even with a single dose administered 2 weeks before infection with a lethal IAV inoculum. Moreover, PSL2-targeting LNAs also enable the surviving mice to develop vigorous immunity. In therapeutic models, a single LNA dose given 3 d after infection provides complete protection from death. Together, these results have exciting implications for the development of a new class of pan-genotypic, anti-IAV therapies for prophylaxis of, treatment of established and 'just-in-time' universal vaccination against an IAV infection. In addition, because traditional vaccines take weeks to provide full protection, a co-administered single dose of LNA14 could provide protection during this vulnerability window.

We envision several paths to the clinic for PSL2-targeted therapies like LNA14 against IAV, including aerosol delivery to outpatients or intravenous administration for severely ill hospitalized patients. Importantly, incorporating the virus's RNA secondary structure into the LNA design allowed us to achieve far greater inhibition than ASOs designed against the same viral genomic sequence, but which relied only on primary nucleotide sequence homology for their design³⁷.

Although we initially focused on IAV, an analogous approach can be taken for virtually any virus of interest. Indeed, we were able to rapidly identify highly conserved RNA secondary structures in SARS-CoV-2 (ref. 30) and then design appropriate LNAs leveraging the lessons learned in targeting IAV—a process we now term 'programmable antivirals'. Our lead LNAs demonstrated greater in vitro activity against SARS-CoV-2 than the nucleoside analog-positive controls at $200\times$ the LNA concentration. Moreover, the LNAs were highly effective against a clinical isolate harboring mutations that have been associated with decreased susceptibility to recent

COVID-19 vaccines³³, with titer reductions of up to 5log₁₀ at 25 nM concentrations of LNA. Finally, our top anti-SARS-CoV-2 LNA exhibited profound *in vivo* activity by successfully decreasing and in some cases completely preventing virus transmission in hamsters. Limitations of our study include the very preliminary nature of the SARS-CoV-2 data and the need for further experiments, including assessment of therapeutic application of the LNA (which is the subject of another paper).

Taken together, this programmable antiviral strategy now excitingly offers a highly adaptable potential solution to current and future viruses of concern, especially respiratory pandemic viruses. Their broad-spectrum potential can enable advanced stockpiling and prepositioning, with the ability to fill the void before a possible vaccine might be developed and deployed. Programmable antivirals can also offer protection against vaccine-resistant virus strains, as well as provide immediate protection during the months needed for vaccine-induced immunity to ramp up.

Online content

Any methods, additional references, Nature Research reporting summaries, source data, supplementary information, acknowledgements, peer review information; details of author contributions and competing interests; and statements of data and code availability are available at <https://doi.org/10.1038/s41591-022-01908-x>.

Received: 21 March 2017; Accepted: 20 June 2022;

Published online: 18 August 2022

References

- Memoli, M. J., Hrabal, R. J., Hassantoufighi, A., Eichelberger, M. C. & Taubenberger, J. K. Rapid selection of oseltamivir- and peramivir-resistant pandemic H1N1 virus during therapy in 2 immunocompromised hosts. *Clin. Infect. Dis.* **50**, 1252–1255 (2010).
- Hai, R. et al. Influenza A (H7N9) virus gains neuraminidase inhibitor resistance without loss of *in vivo* virulence or transmissibility. *Nat. Commun.* **4**, 2854 (2013).
- Hayden, F. G. & de Jong, M. D. Emerging influenza antiviral resistance threats. *J. Infect. Dis.* **203**, 6–10 (2011).
- Romero-Lopez, C. & Berzal-Herranz, A. Unmasking the information encoded as structural motifs of viral RNA genomes: a potential antiviral target. *Rev. Med. Virol.* **23**, 340–354 (2013).
- Pang, P. S. et al. Structural map of a microRNA-122: hepatitis C virus complex. *J. Virol.* **86**, 1250–1254 (2012).
- Palese, P. & Shaw, M. L. Orthomyxoviridae. In *Fields Virology* 5th edn (eds Knipe, D. M. & Howley, P. M.) 1647–1689 (Lippincott Williams & Wilkins, 2007).
- Compans, R. W., Content, J. & Duesberg, P. H. Structure of the ribonucleoprotein of influenza virus. *J. Virol.* **10**, 795–800 (1972).
- Noda, T. & Kawaoka, Y. Structure of influenza virus ribonucleoprotein complexes and their packaging into virions. *Rev. Med. Virol.* **20**, 380–391 (2010).
- Hutchinson, E. C., von Kirchbach, J. C., Gog, J. R. & Digard, P. Genome packaging in influenza A virus. *J. Gen. Virol.* **91**, 313–328 (2010).
- Gao, Q. et al. The influenza A virus PB2, PA, NP, and M segments play a pivotal role during genome packaging. *J. Virol.* **86**, 7043–7051 (2012).
- Marsh, G. A., Rabadan, R., Levine, A. J. & Palese, P. Highly conserved regions of influenza A virus polymerase gene segments are critical for efficient viral RNA packaging. *J. Virol.* **82**, 2295–2304 (2008).
- Fournier, E. et al. A supramolecular assembly formed by influenza A virus genomic RNA segments. *Nucleic Acids Res.* **40**, 2197–2209 (2012).
- Gavazzi, C. et al. An *in vitro* network of intermolecular interactions between viral RNA segments of an avian H5N2 influenza A virus: comparison with a human H3N2 virus. *Nucleic Acids Res.* **41**, 1241–1254 (2013).
- Gog, J. R. et al. Codon conservation in the influenza A virus genome defines RNA packaging signals. *Nucleic Acids Res.* **35**, 1897–1907 (2007).
- Moss, W. N., Priore, S. F. & Turner, D. H. Identification of potential conserved RNA secondary structure throughout influenza A coding regions. *Rna* **17**, 991–1011 (2011).
- Liang, Y., Huang, T., Ly, H. & Parslow, T. G. Mutational analyses of packaging signals in influenza virus PA, PB1, and PB2 genomic RNA segments. *J. Virol.* **82**, 229–236 (2008).
- Muramoto, Y. et al. Hierarchy among viral RNA (vRNA) segments in their role in vRNA incorporation into influenza A virions. *J. Virol.* **80**, 2318–2325 (2006).
- Wilkinson, K. A., Merino, E. J. & Weeks, K. M. Selective 2'-hydroxyl acylation analyzed by primer extension (SHAPE): quantitative RNA structure analysis at single nucleotide resolution. *Nat. Protoc.* **1**, 1610–1616 (2006).
- Pang, P. S., Elazar, M., Pham, E. A. & Glenn, J. S. Simplified RNA secondary structure mapping by automation of SHAPE data analysis. *Nucleic Acids Res.* **39**, e151 (2011).
- Priore, S. F., Moss, W. N. & Turner, D. H. Influenza A virus coding regions exhibit host-specific global ordered RNA structure. *PLoS ONE* **7**, e35989 (2012).
- Kladwang, W. & Das, R. A mutate-and-map strategy for inferring base pairs in structured nucleic acids: proof of concept on a DNA/RNA helix. *Biochemistry* **49**, 7414–7416 (2010).
- Tian, S., Cordero, P., Kladwang, W. & Das, R. High-throughput mutate-map-rescue evaluates SHAPE-directed RNA structure and uncovers excited states. *RNA* **20**, 1815–1826 (2014).
- Vester, B. & Wengel, J. LNA (locked nucleic acid): high-affinity targeting of complementary RNA and DNA. *Biochemistry* **43**, 13233–13241 (2004).
- Kurreck, J., Wyszko, E., Gillen, C. & Erdmann, V. A. Design of antisense oligonucleotides stabilized by locked nucleic acids. *Nucleic Acids Res.* **30**, 1911–1918 (2002).
- Straarup, E. M. et al. Short locked nucleic acid antisense oligonucleotides potently reduce apolipoprotein B mRNA and serum cholesterol in mice and non-human primates. *Nucleic Acids Res.* **38**, 7100–7111 (2010).
- Staedel, C. et al. Inhibition of gastric tumor cell growth using seed-targeting LNA as specific, long-lasting microRNA inhibitors. *Mol. Ther. Nucleic Acids* **4**, e246 (2015).
- Javanbakht, H. et al. Liver-targeted anti-HBV single-stranded oligonucleotides with locked nucleic acid potently reduce HBV gene expression *in vivo*. *Mol. Ther. Nucleic Acids* **11**, 441–454 (2018).
- Hillebrand, F. et al. Gymnotic delivery of LNA mixmers targeting viral SREs induces HIV-1 mRNA degradation. *Int. J. Mol. Sci.* **20**, 1088 (2019).
- Influenza Treatment* (Centers for Disease Control and Prevention, National Center for Immunization and Respiratory Diseases, 2019).
- Rangan, R. et al. RNA genome conservation and secondary structure in SARS-CoV-2 and SARS-related viruses: a first look. *RNA* **26**, 937–959 (2020).
- Sheahan, T.P., et al. An orally bioavailable broad-spectrum antiviral inhibits SARS-CoV-2 in human airway epithelial cell cultures and multiple coronaviruses in mice. *Sci. Transl. Med.* **12**, abb5883 (2020).
- Wang, R. et al. Genetic screens identify host factors for SARS-CoV-2 and common cold coronaviruses. *Cell* **184**, 106–119.e114 (2021).
- SARS-CoV-2 Variant Classifications and Definitions* (Centers for Disease Control & Prevention, National Center for Immunization and Respiratory Diseases, Division of Viral Diseases, 2022); <https://www.cdc.gov/coronavirus/2019-ncov/variants/variant-classifications.html>
- Bloom, J. D., Gong, L. I. & Baltimore, D. Permissive secondary mutations enable the evolution of influenza oseltamivir resistance. *Science* **328**, 1272–1275 (2010).
- Takashita, E. et al. Detection of influenza A (H3N2) viruses exhibiting reduced susceptibility to the novel cap-dependent endonuclease inhibitor baloxavir in Japan. *Eur. Surveill.* **24**, 1800698 (2019).
- Hurt, A. C. et al. Characteristics of a widespread community cluster of H275Y oseltamivir-resistant A(H1N1)pdm09 influenza in Australia. *J. Infect. Dis.* **206**, 148–157 (2012).
- Giannechini, S., Clausi, V., Nosi, D. & Azzi, A. Oligonucleotides derived from the packaging signal at the 5' end of the viral PB2 segment specifically inhibit influenza virus *in vitro*. *Arch. Virol.* **154**, 821–832 (2009).

Publisher's note Springer Nature remains neutral with regard to jurisdictional claims in published maps and institutional affiliations.

© The Author(s), under exclusive licence to Springer Nature America, Inc. 2022

Methods

Cells and viruses. HEK293T (CRL-1573), Vero E6 (CRL-1586) and MDCK-NLB-2 (CCL-34) cells were obtained from American Type Culture Collection (ATCC) and were maintained according to ATCC instructions. A549-Dual (a549d-nfs) and THP1-Dual (thpd-nfs) were obtained from InvivoGen and maintained according to the manufacturer's instructions. All cell lines used in the present study were routinely checked for *Mycoplasma* contamination (MycoAlert Mycoplasma Detection Kit, Lonza) and were authenticated by the respective vendors. All cell lines used for SARS-CoV-2 experimentation, including Huh-7, ACE2-TMPRSS2-Huh-7.5 and ACE2-A549 cells, were maintained at 37 °C in complete Dulbecco's modified Eagle's medium (DMEM; Gibco) containing 10% fetal bovine serum (FBS; Invitrogen), penicillin and streptomycin (Gibco) and Hepes buffer (Gibco). The ACE2-A549 cells were specially engineered to overexpress the ACE2 receptor in human alveolar basal epithelial cells (A549), whereas the ACE2-TMPRSS2-Huh-7.5 cells were a kind gift of the Catherine Blish laboratory and engineered to overexpress both ACE2 and human TMPRSS2 receptors. A549-Dual and THP1-Dual cells were purchased from InvivoGen.

WT influenza A/PR/8/34 (PR8) H1N1 virus (ATCC-VR-95) and the tissue-culture-adapted PR8 virus (ATCC-VR-1469) were purchased from ATCC. PR8 mutant viruses were generated using an eight-plasmid reverse genetic system as previously described³⁸. Tissue-cultured adapted influenza A/Hong Kong/8/68 (HK68) H3N2 virus (ATCC-VR-1679), A/Virginia/ATCC6/2012 (H3N2) virus (ATCC-VR-1811), A/Virginia/ATCC1/2009TC (H1N1) virus (ATCC-VR-1736) and A/Wisconsin/33 (H1N1) virus (VR-1520) were purchased from ATCC. A/California/4/2009 (pH1N1) virus was kindly gifted by E. Govorkova from St. Jude Children's Research Hospital (Memphis, USA). Viruses were grown and amplified in 10-d-old, specific, pathogen-free, research-grade chicken embryos at 35 °C (Charles River Laboratories; SPAEAS).

WT recombinant SARS-CoV-2 was prepared and handled as described³⁹. The recombinant SARS-CoV-2-Nluc virus is an authentic, fully replicating virus in which ORF7a has been deleted and replaced with Nluc⁴⁰. The SARS-CoV-2 clinical variant was isolated from a 54-year-old man with melanoma and lymphoma, who received a confirmed COVID-19 diagnosis by PCR in March 2020. Virus sequencing was performed on virus isolated from a nasopharyngeal swab sample in virus transport medium taken after the patient had been infected for 7 months.

Plasmid constructs and cloning. Plasmids were used containing the WT *PB2* segments from influenza viruses A/Puerto Rico/8/34 (H1N1) (PR8), A/New York/470/2004 (H3N2) (NY470), A/New York/312/2001 (H1N1) (NY312), A/Brevig Mission/1/1918 (H1N1) (1918), A/California/04/2009 (H1N1) (CA09) and A/Vietnam/03/2004 (H5N1) (VN1203). For the generation of PR8 packaging mutant vRNA, we utilized a Stratagene QuickChange XL site-directed mutagenesis kit for mutagenesis of a pDZ plasmid containing the *PB2* gene of PR8 (ref. ³⁸). Sequences of each mutated construct were confirmed by automated sequencing. The eight-plasmid pBD rescue system for A/WSN/33 (H1N1) was kindly donated by A. Mehle. The H275Y NA mutant was generated by QuickChange mutagenesis from the bidirectional pBD plasmids, as described above.

Reverse genetics and virus titrations. Recombinant A/Puerto Rico/8/34 (PR8) virus and recombinant A/WSN/33 (WSN) virus were generated using eight-plasmid reverse genetic systems³⁸. Briefly, 1×10^6 cells of a HEK293T/MDCK co-culture were Lipofectamine 3000 (Invitrogen) transfected with 1 µg of one of each of the eight segments contained within plasmids that utilize a bidirectional dual Pol I/II promoter system for the simultaneous synthesis of genomic vRNA and messenger RNA. For rescue of compensatory *PB2* mutant viruses where a nonsynonymous change was required, a WT *PB2* protein expression plasmid (Pol II) was co-transfected during virus rescue. Supernatants were collected 24 h post-transfection. PR8 rescue viruses were then inoculated into the allantoic cavities of 10-d-old chicken embryos. WSN rescue viruses were passaged subsequent times on MDCK cells. Rescue of recombinant viruses was assessed by hemagglutination (HA) activity. Each newly rescued virus was further plaque titered and mutations were confirmed by sequencing of mutated genes. Plaque assays were carried out on confluent MDCK cells as described previously⁴¹. HA assays were carried out in 96-well round-bottomed plates at room temperature, using 50 µl of virus dilution and 50 µl of a 0.5% suspension of turkey red blood cells (LAMPIRE Biological Laboratories) in PBS.

Isolation of packaged vRNAs. To analyze packaged vRNA for PR8 mutated viruses, 10-d-old eggs were inoculated with approximately 1,000 p.f.u. of recombinant virus and incubated for 72 h. Allantoic fluid was harvested and supernatant was dual clarified by low-speed centrifugation. Clarified supernatant was then layered on a 30% sucrose cushion and ultracentrifuged at 30,000 r.p.m. for 2.5 h (Beckman Rotor SW41). Pelleted virus was resuspended in PBS and TRIzol (Invitrogen) extracted. Precipitated vRNA was resuspended in a final volume of 20 µl of 10 mM Tris-HCl, pH 8.0 and stored at -80 °C. Virus supernatant from LNA-treated cells was harvested 48 h post-infection and subjected to low-speed centrifugation at 1,000 r.p.m., then 10,000 r.p.m. Isolation continued as indicated above.

Quantitative PCR analysis of packaged vRNAs. Approximately 200 ng of extracted vRNA was reverse transcribed using a universal 3'-primer (5'-AGGGCTCTTCGCCAGCRAAAGCAGG) and Superscript III reverse transcriptase (Invitrogen). The reverse transcription (RT) product was diluted approximately 10,000-fold and used as a template for quantitative (q)PCR. Separate PCRs were then carried out as previously described⁴² with segment-specific primers. The 10-µl reaction mixture contained 1 µl of diluted RT product, a 0.5 µM primer concentration and SYBR Select Master Mix (Applied Biosystems) which included SYBR GreenER dye, 200 µM deoxynucleoside triphosphates, heat-labile UDG (uracil-*N*-glycosylase), optimized SYBR Green Select Buffer and AmpliTaq DNA polymerase UP enzyme. Relative vRNA concentrations were determined by analysis of cycle threshold values, total vRNA amount within a sample was normalized to the level of HA vRNA and then percentages of incorporation were calculated relative to the levels of WT vRNA packaging. Viral packaging results represent the averaged levels of vRNA incorporation \pm s.d. derived from two independent virus purifications, with vRNA levels quantified in triplicate.

Denaturing RNA gel. Extracted viral RNA (100–300 ng) was diluted with equal volume of NOVEX TBE-Urea sample buffer and incubated at 70 °C for 10 min before separation on a 6% TBE-Urea gel for 18 h at a constant voltage of 80 V. RNA from each sample was run in several dilutions to enable clear visualization of the genomic RNA without over-saturation of the band's signal. The RNA was visualized by staining for 30 min in 0.5x Tris/borate/EDTA (TBE) buffer supplemented with 0.5 mg ml⁻¹ of ethidium bromide followed by visualization in a GelDoc EZ Imager system (BioRad). Silver staining was performed using the SilverXpress silver stain kit (Invitrogen) according to the manufacturer's instruction. Silver staining and ethidium bromide staining were compared and shown to have the same linear range of detection (data not shown); ethidium bromide was selected for lane visualization due to a higher background signal in silver staining. The band intensity in each lane was determined using Image Lab Software (BioRad) and an analysis of the intensity of each genomic band relative to the total intensity of all genome segments was determined and normalized to the intensity of the HA band relative intensity.

Strand-specific RT-qPCR. MDCK cells transfected with 1 M LNA9 or Scr. LNA were infected with PR8 virus at an MOI of 0.1 24 h post-transfection. Then 8 h post-infection total cellular RNA was extracted in TRIzol reagent (Invitrogen) and the RNA was purified using the Direct-Zol RNA mini-prep (Zymo Research) according to the manufacturer's protocol. RT and qPCR were performed according to the literature⁴³. Complementary DNAs of the influenza vRNA and complementary viral RNA (cRNA) were synthesized with tagged primers to add an 18- to 20-nt tag that was unrelated to the influenza virus at the 5'-end (cRNA tag: 5'-GCT AGC TTC AGC TAG GCA TC-3'; vRNA tag: 5'-GGC CGT CAT GGT GGC GAA T-3'). Hot-start RT with the tagged primer was performed as described in Kawakami et al.⁴³ using saturated trehalose. A 5.5-µl mixture containing 200 ng of total RNA sample and 10 pmol of tagged primer was heated for 10 min at 65 °C, chilled immediately on ice for 5 min and then heated again at 60 °C. After 5 min, 14.5 µl of preheated reaction mixture (4 µl of First Strand buffer (5x, Invitrogen), 1 µl of 0.1 M dithiothreitol, 1 µl of dNTP mix (10 mM each), 1 µl of Superscript III reverse transcriptase (200 U µl⁻¹, Invitrogen), 1 µl of RNasin Plus RNase inhibitor (40 U µl⁻¹, Promega) and 6.5 µl of saturated trehalose) was added and incubated for 1 h. RT-qPCR was performed with PowerUp SYBR Green SuperMix (Applied Biosystems) on a BioRad CFX96 Real-Time System. Then 7 µl of a tenfold dilution of the cDNA was added to the qPCR reaction mixture (10 µl of SYBR Green SuperMix (2x), 1.5 µl of forward primer (10 µM) and 1.5 µl of reverse primer (10 µM)). The cycle conditions of qPCR were 95 °C for 10 min, followed by 40 cycles of 95 °C for 15 s and 60 °C for 1 min. The qPCR primers were: PR8 segment 1 (*PB2*) cRNA: forward: 5'-TCC ACC AAA GCA AAG TAG AAT GC-3'; reverse: 5'-GCT AGC TTC AGC TAG GCA TCA GTA GAA ACA AGG TCG TTT TTA AAC-3'; PR8 segment 1 (*PB2*) vRNA: forward: 5'-GGC CGT CAT GGT GGC GAA TAG ACG AAC AGT CGA TTG CCG AAG C-3', reverse: 5'-AGT ACT CAT CTA CAC CCA TTT TGC-3'; PR8 segment 4 (*HA*) cRNA: forward: 5'-CTG TAT GAG AAA GTA AAA AGC C-3', reverse: 5'-GCT AGC TTC AGC TAG GCA GTA GAA ACA AGG GTG TTT TTC-3'; and PR8 segment 4 (*HA*) vRNA: forward: 5'-GGC CGT CAT GGT GGC GAA TAG GAT GAA CTA TTA CTG GAC CTT GC-3', reverse: 5'-TCC TGT AAC CAT CCT CAA TTT GGC-3'.

Animals. All animal studies were performed in accordance with the National Institutes of Health Guidelines for the Care and Use of Laboratory Animals and approved by the Stanford University Administrative Panel on Laboratory Animal Care and by the Utah State University Institutional Animal Care and Use Committee. Animals were housed in disposable cages connected to an Innorack IVC-ventilated rodent housing system under 12 h light:dark cycle at 24 °C and 25–30% humidity. Healthy age-matched female BALB/c mice aged 6–8 weeks (Jackson Laboratories) were randomly separated into groups for infection/treatment or used as uninfected/nontreated controls. Treatment groups were not blinded to the investigators. Mice were identified with tag numbers throughout the experiment. The 10-week-old female golden Syrian hamsters (LVG strain,

Charles River Laboratories) were separated into groups for exposure studies with an additional sentinel group that was inoculated directly with virus.

In vivo mouse infections. Mice were lightly anesthetized with isoflurane and intranasally infected with 50 μ l of virus preparation at 1 LD₅₀—a concentration of approximately 1,000 p.f.u. for virus-packaging mutant experiments and 900 p.f.u. for LNA treatment experiments. Weights and clinical scores were assessed daily, and animals were humanely sacrificed when a clinical score of 5 was recorded (see Supplementary Table 2 for clinical score determination). Kaplan–Meier survival curves were generated using GraphPad Prism.

In vivo mouse IAV antiviral assays. ‘In vivo-ready’ LNAs were custom designed and ordered from QIAGEN (formally Exiqon) and later from IDT. For intranasal delivery, in vivo-ready LNA was mixed in complexes with in vivo-JetPEI transfection reagent (Polyplus) according to the manufacturer’s protocol to the indicated final concentration in 50–75 μ l of 5% glucose solution. Mice were then lightly anesthetized with isoflurane and 50–75 μ l of the solution was delivered intranasally. For retro-orbital delivery, in vivo-ready LNA was mixed in complexes with in vivo-JetPEI transfection reagent (Polyplus) according to the manufacturer’s protocol to the indicated final concentration in 200 μ l of 5% glucose solution. Mice were then anesthetized and the solution was delivered by retro-orbital injection. OSLT (Sigma-Aldrich, catalog no. SML1606) was prepared in sterile water and administered to mice at a dose of 10 mg kg⁻¹ twice daily by oral gavage (totaling 20 mg kg⁻¹ d⁻¹), with 8 h between dosing intervals.

Prevention of SARS-CoV-2 transmission in Syrian hamsters. Infection of donor sentinel hamsters (nontreated): 6-week-old WT golden Syrian hamsters were intranasally infected with 1 \times 10^{3.3} CCID₅₀ (cell culture infectious dose 50%) of SARS-CoV-2 (USA_WA1/2020 strain) in a 100- μ l volume. LNA pretreatment group: 6-week-old golden Syrian hamsters (n = 5) were pretreated by intranasal instillation with a 200- μ l volume containing 100 μ g of LNA-12.8 on day –1 and day 0 before exposure to the SARS-CoV-2-infected sentinel hamsters. Vehicle-treated hamsters (n = 4) received PBS by intranasal nebulization. LNA- and vehicle-treated hamsters were co-housed and exposed to the infected sentinels for 2 h per d for 3 consecutive days. Then, 4 d after the initial exposure, the lungs were harvested and virus titers were determined by CCID₅₀ in triplicate. Statistical analysis was performed using an unpaired Student’s *t*-test with GraphPad Prism 9 software.

LNA design and preparation. Oligonucleotides containing LNAs were custom synthesized by Exiqon and later by IDT. Capitalized letters denote LNA. Lower-case letters denote typical (nonlocked) DNA nucleotides. All oligonucleotides contain phosphorothioate internucleoside linkages. LNA8 and -9 were designed as LNA gapmers to contain a stretch of six or seven DNA nucleotides optimized for RNase-H recruitment. Sequences of all LNAs are shown below:

LNA1: 5′-AccAaaAGaaT-3′

LNA2: 5′-TggCcATcaaT-3′

LNA3: 5′-TagCAatActtA-3′

LNA4: 5′-CCAAAAGA-3′

LNA5: 5′-CATACTTA-3′

LNA6: 5′-CagaCaCGaCCaaAA-3′

LNA7: 5′-TAcTtAcTgaCagCC-3′

LNA8: 5′-AGAcagacacaaAAG-3′

LNA9: 5′-TACTTactgacaGCC-3′

LNA14: 5′-CGACcaaaagaATTTC-3′

Scr. LNA (negative control): 5′-AACACGTCTATACGC-3′

SARS-CoV-2-directed LNAs:

LNA-12.8: 5′-AGGAagttgtagCAGC-3′

LNA-14.3: 5′-GCTtccatcttaCCT-3′

In vitro LNA antiviral assays. For all experiments, LNAs were reconstituted in RNase-free water at 100 μ M stock solutions, aliquoted and stored at –20 °C before single use. Lipofectamine 3000 (Life Technologies) was used to transfect LNA into cells at indicated concentrations per the manufacturer’s protocol.

For IAV prophylactic antiviral assays, 1 \times 10⁶ MDCK cells were plated in 6-well plates 24 h before being transfected with the indicated LNA. Cells were then infected at the indicated time points with 0.01 MOI of PR8 (H1N1) or HK68 (H3N2) virus. For post-infection therapeutic assessment, MDCK cells were infected with PR8 or HK68 before LNA transfection as described above. Then 48 h post-infection, supernatant was collected and the viral titer was determined by plaque assay in triplicate.

For SARS-CoV-2-Nluc assays: 1 d before transfection, Huh-7 or ACE2-TMPRSS2-Huh-7.5 was plated on 96-well clear-bottomed plates to 60–70% confluency at the time of treatment with the LNA ASOs LNA-12.8, LNA-14.3 or Scr. LNA. Lipofectamine 3000 (Life Technologies) was used to transfect LNA ASOs into cells at 25 nM or 100 nM final concentration, according to the manufacturer’s protocol. Cells were then infected with SARS-CoV-2 reporter virus expressing nanoluciferase (SARS-CoV-2-Nluc) at an MOI of 0.3 for 1 h, after which the virus was removed and fresh medium was added. Recombinant SARS-CoV-2-Nluc

is a fully replicating virus in which ORF7 has been deleted and replaced with Nluc. Thus, the measurement of Nluc expression is a surrogate marker of virus replication enabling the screening of antiviral compounds. A nucleoside analog β -D-N⁴-hydroxycytidine, EIDD-1931, with potent activity against SARS-CoV-2, was included as a positive control. A DMSO control was included as a mock-treated, negative control. Data were graphed and analyzed in Prism v.8 and v.9 by GraphPad. Statistical analysis of the data from each cell type was computed as an ordinary one-way analysis of variance (ANOVA) using Dunnett’s multiple comparison test against the DMSO control or Scr. LNA control from each cell type, where indicated.

SARS-CoV-2 plaque assay experiments were performed in 24-well plates: 24-well plates were seeded with 1 \times 10⁵ Vero E6 cells per well in DMEM, 10% FBS and 1 \times antibiotic/antimycotic 24 h before Lipofectamine 3000 transfection of LNA. Scr. LNA was included as a negative control. Then 12 h post-transfection, LNA-transfection medium was removed, and cells were infected at an MOI of 0.01 with either recombinant WT SARS-CoV-2 (PMID: 32526206) or a SARS-CoV-2 clinical isolate derived from a nasopharyngeal swab taken from a chronically infected cancer patient 7 months after the initial confirmatory COVID-19 PCR test. After adding virus inoculum, plates were incubated at 37 °C for 1 h, after which input virus was removed, wells were washed with 1 ml of medium and 1 ml of ‘infection medium’ (DMEM, 5% FBS, 1 \times antibiotic/antimycotic) was added. After 48 h at 37 °C, 200 μ l of culture supernatant was collected and stored at –80 °C until quantitation of infectious virus by plaque assay. Briefly, Vero E6 cells were seeded at 500,000 cells per well per 2 ml in 6-well plates. After 24 h, samples were thawed at room temperature and serially diluted in PBS. Medium was removed from the six-well plates and serial dilutions were added to the plate, incubated for 1 h at 37 °C and then overlaid with DMEM, 5% FBS, 1 \times antibiotic/antimycotic and 0.9% agarose. After 72 h, neutral red stain was added to each plate, incubated for 3 h and plaques were counted. The number of plaque-forming units (p.f.u.) per milliliter was generated using the following formula: p.f.u. ml⁻¹ = number of plaques \times serial dilution factor \times 5.

LNA treatment and IAV-packaging efficiency determination. Briefly, T75 flasks of 80% confluent MDCK cells were transfected with 100 nM of Scr. LNA, LNA9 or mock untreated by Lipofectamine 3000 transfection, according to the manufacturer’s protocol. Then 12 h post-transfection, cells were infected with 0.01 MOI of WT TC-adapted PR8 virus. After 1 h, virus was removed and the cells were washed with PBS; 48-h post-infection supernatants were collected and RNA was isolated as described in isolation of packaged vRNAs and assay methods.

In vitro drug selection. LNA9 selection: 80–90% confluent MDCK cells in 12-well plates were transfected in duplicate with a starting concentration of 0.01 nM (~1/2 EC₅₀) LNA9 for passage 1 by Lipofectamine transfection (see above). Then 12 h post-transfection, cells were washed with PBS and infected with an MOI of 0.01 of WT PR8 virus. After 1-h incubation at 37 °C, cells were washed and virus growth medium was added. Cells were incubated until 50% cytopathic effect (CPE) was evident (48–72 h). Virus supernatant was harvested, low-speed centrifuge clarified, aliquoted, plaque titered and stored at –80 °C. The virus supernatant was then continuously serially passaged in the presence of escalating concentrations of LNA9 (0.01 nM to 100 nM). If no CPE were evident, the drug concentration was lowered and the added virus concentration increased until 50% CPE occurred. OSLT selection: confluent MDCK cells in 12-well plates were infected with an MOI of 0.01 of PR8 virus. After adsorption for 1 h, cells were washed with PBS and OSLT (Sigma-Aldrich, catalog no. Y0001340) was added to the virus growth medium at a starting concentration of 1 nM (~1/2 EC₅₀). Drug selection proceeded as described above, with escalating concentrations of OSLT (0.01 nM to 250 μ M) at each subsequent passage.

EC₅₀ determination. For LNA9, the EC₅₀ was defined as the concentration of drug effective in reducing the percentage of virus titer to 50% of that for the no-drug control. In brief, the EC₅₀ was determined by seeding 5 \times 10⁵ MDCK cells in each well of a 12-well plate and incubating overnight at 37 °C under 5% CO₂. Cells were then transfected with LNA9 as described above at concentrations from 0.01 nM to 10 μ M. Plates were incubated at 37 °C for 12 h before infection with 0.01 MOI of WT PR8, serially passaged LNA-treated virus, WSN33 WT or WSN33 H275Y NAI-resistant virus. Then 48 h post-infection, supernatants were collected, centrifuge clarified, aliquoted and stored at –80 °C. The viral titer for each drug dilution was performed by plaque assay in duplicate. The EC₅₀ was the concentration of LNA9 yielding a percentage titer of 50% of that without drug.

For OSLT, the EC₅₀ was defined as the concentration of drug reducing the total percentage of plaques to 50% of that for the no-drug control, determined by plaque reduction assay³. Briefly, confluent MDCK cells in 12-well plates were infected with approximately 100 p.f.u. of WT PR8, serially passaged OSLT-treated virus, WSN33 WT or WSN33 H275Y NAI-resistant virus and incubated for 1 h at 37 °C. Cells were then washed with PBS and a 50:50 mix of 1% agarose: 2 \times virus growth DMEM containing varying concentrations of drug (0.1 nM to 1 mM) was added to the cells. Plates were harvested 72 h later, stained with Crystal Violet and plaques were counted. The EC₅₀ was the concentration of OSLT reducing the

total percentage of plaques to 50% of that without drug. All results were plotted in GraphPad Prism to generate EC₅₀ curves.

In vitro transcription of full-length IAV vRNA. For each WT isolate (PR8, 1918, VN1203, NY470, NY312 and CA09) and PR8 packaging mutant clones, *PB2* cDNA was amplified from plasmid using, segment-specific primers under a T7 promoter. Amplified cDNA was gel purified using an Invitrogen DNA gel kit. The vRNAs were then produced by in vitro transcription, using T7-MEGAScript kit. The vRNAs for SHAPE were purified by MEGAClear (Thermo Fisher Scientific, catalog no. AM1908) with purity and length verified by capillary electrophoresis.

The single fluorophore-SHAPE 1D analysis of full-length IAV vRNA. In vitro transcribed *PB2* vRNA was folded (100 mM NaCl, 2.5 mM MgCl₂, 65 °C for 1 min, 5-min cooling at room temperature, 37 °C for 20–30 min) in 100 mM Hepes, pH 8. The 2'-acylation with *N*-methylisatoic anhydride¹⁸ and RT primer extension were performed at 45 °C for 1 min, 52 °C for 25 min and 65 °C for 5 min, as previously described⁴⁴. 6-Carboxyfluorescein (6FAM) was used for all labeled primers (primer sequences available on request). Exceptions to these protocols were as follows: (1) RNA purification after acylation was performed using RNA C&C columns (Zymo Research), rather than ethanol precipitation; (2) before and after SHAPE primer buffer was added, the mixture was placed at room temperature for 2–5 min, which enhanced RT yields significantly; (3) DNA purification was performed using Sephadex G-50 size exclusion resin in 96-well format, then concentrated by vacuum centrifugation, resulting in a more significant removal of primer; and (4) 2 pmol of RNA was used in ddGTP (2',3'-dideoxyguanosine-5'-triphosphate) RNA-sequencing reactions.

The ABI 3100 Genetic Analyzer (50-cm capillaries filled with POP-6 matrix) was set with the following parameters: voltage 15 kV, *T* = 60 °C, injection time = 15 s. The GeneScan program was used to acquire the data for each sample, which consisted of purified DNA resuspended in 9.75 μl of Hi-Di-Formamide, to which 0.25 μl of ROX500 internal size standard (ABI catalog no. 602912) was added. PeakScanner parameters were set to the following parameters: smoothing=none; window size=25; size calling=local southern; baseline window=51; peak threshold=15. Fragments 250 and 340 were computationally excluded from the ROX500 standard⁴⁵. The data from PeakScanner were then processed into SHAPE data by using FAST (fast analysis of SHAPE traces), a customized algorithm developed in our lab¹⁹. FAST automatically corrects for signal differences due to handling errors, adjusts for signal decay and converts fragment length to nucleotide position, using a ddGTP ladder as an external sizing standard and the local Southern blotting method^{31,19}. This algorithm embedded in the RNAstructure program is freely available at <http://med.stanford.edu/glennlab/download.html>.

RNAstructure parameters: slope and intercept parameters of 2.6 and -0.8 kcal mol⁻¹ were initially tried, as suggested⁴⁶; however, we found that smaller intercepts closer to 0.0 kcal mol⁻¹ (for example, ~-0.3) produced fewer less optimal structures (within a maximum energy difference of 10%). We speculate that this minor parameter difference may be due to the precise fitting achieved between experimental and control datasets by the automated FAST algorithm. FAST was written in ANSI C/C++ and is integrated into RNAstructure with FAST, which requires MFC (Microsoft Foundation Classes). RNA structures were drawn and colored using RNAviz 2 (ref. 47) and finalized in Adobe Illustrator.

IAV PSL2 construct design, RNA synthesis and chemical modification for M² experiments. Double-stranded DNA templates were prepared by PCR assembly of DNA oligomers designed by an automated MATLAB script as previously described (available at <https://primerize.stanford.edu>)⁴⁸. Constructs for M² include all single mutants to the Watson-Crick counterpart. Compensatory mutants for M²R were designed based on basepairing in the proposed secondary structure²². In vitro transcription reactions, RNA purification and quantification steps were as described previously¹⁸. One-dimensional (1D) chemical mapping, M² and M²R were carried out in the 96-well format as described previously^{48–50}. Briefly, RNA was heated up and cooled to remove secondary structure heterogeneity, then folded properly and incubated with SHAPE reagent (5 mg ml⁻¹ of 1-methyl-7-nitroisatoic anhydride (1M7))³¹; modification reaction was quenched and RNA was recovered by poly(dT) magnetic beads (Ambion) and FAM-labeled Tail2-A20 primer; RNA was washed by 70% ethanol twice and resuspended in double-distilled water (ddH₂O), followed by RT to cDNA and heated NaOH treatment to remove RNA. The final cDNA library was recovered by magnetic bead separation, rinsed, eluted in Hi-Di-Formamide (Applied Biosystems) with ROX350 ladder and loaded to a capillary electrophoresis sequencer (ABI 3100). Data processing, structural modeling and data deposition: the HiTRACE software package v.2.0 was used to analyze CE data (both MATLAB toolbox and web server available^{52,53}). Trace alignment, baseline subtraction, sequence assignment, profile fitting, attenuation correction and normalization were accomplished as previously described^{54,55}. Sequence assignment was accomplished manually with verification from sequencing ladders. Data-driven secondary structure models were obtained using the Fold program of the RNAstructure package v.5.4 (ref. 56) with pseudo-energy slope and intercept parameters of 2.6 kcal mol⁻¹ and -0.8 kcal mol⁻¹. Two-dimensional *z*-score matrices for M² datasets and helix-wise bootstrapping

confidence values were calculated as described previously^{22,48}. The *z*-score matrices were used as basepair-wise, pseudo-free energies with a slope and intercept of 1.0 kcal mol⁻¹ and 0 kcal mol⁻¹. Secondary structure images were generated by VARNA⁵⁷. These chemical-mapping datasets, including 1D mapping, M² and M²R have been deposited at the RNA Mapping DataBase (RMDb: <http://rmdb.stanford.edu>)⁵⁸, accession nos.: PSL2IAV_1M7_0001, PSL2IAV_RSQ_0001.

SHAPE analysis of LNA-targeted IAV vRNA. A truncated DNA template of PR8 virus segment *PB2* containing nucleotides 1–88 was prepared by PCR assembly of DNA oligomers, and in vitro transcription reactions, RNA purification and quantification steps were as described previously⁴⁸. The 1D SHAPE chemical mapping was performed in a 96-well plate format as described above, with the following exception: once RNA was denatured and refolded as described, 100 nM of each prepared LNA was added to the folded RNA and incubated with 5 mg ml⁻¹ of SHAPE reagent 1M7. Modification quenching, RNA recovery, re-suspension, RT, cDNA-sequencing and data processing were performed as described⁵⁰.

SHAPE 1D analysis of nontreated and LNA-treated SARS-COV-2 RNA. RNA was folded (0.5 M Na Hepes, pH 8; 90 °C for 3 min, 12-min cooling at room temperature, 50 °C for 20 min, 12-min cooling at room temperature) in 100 mM MgCl₂ with or without LNA and with or without SHAPE reagent 1M7 modification. RNA was purified and quenched with magnetic beads (0.5 M 2-(*N*-morpholino)ethanesulfonic acid sodium salt, pH 6, FAM-A20 tail 2 primer, 5 M NaCl and Ampure beads) and reverse transcribed at 48 °C for 40 min, followed by a 0.4 M NaOH acid quench to improve signal intensity. The resulting cDNA was resuspended in ROX Hi-Di-Formamide and diluted for capillary electrophoresis analysis. As an internal control, the RNA was created with GAGUA hairpins in 5' and 3'-termini designed to be reactive in the presence of 1M7. The results were analyzed using the HiTRACE method⁵² and standardized by the Kladwang et al. method⁵⁵.

PBMCs and splenocyte isolation. Whole blood was collected from mice into heparinized tubes. The whole blood was overlaid on top Ficoll-Paque medium and centrifuged at 400g for 40 min at room temperature. The top layer containing plasma and platelets was removed and the peripheral blood mononuclear cells (PBMCs) at the interphase of the Ficoll layer were collected. The mononuclear cells were diluted in PBS and pelleted by centrifugation at 500g for 15 min after an additional wash with PBS. The pellet was suspended in PBS. Splenocytes were isolated by manually grinding the spleen over a 40-μm cell strainer. The cells were transferred several times through the strainer and processed further as described above. TruStain fcX (anti-mouse CD16/32) antibody specific for FcγR III/II (1 μg per 1 × 10⁶ cells) was used to block nonspecific staining, followed by staining with Zombie Aqua viability kit (BioLegend). Antibody staining was performed by mixing the cells with an antibody mix containing BD Horizon PE-CF594 Rat Anti-Mouse CD45 (BD Biosciences), PE/Cy7 anti-mouse CD3 (BioLegend), APC/Cy7 anti-mouse CD8a (BioLegend) and H-2Kd Influenza HA Tetramer-IYSTVASSL-PE (MBL International). All antibodies were diluted at a ratio of 2 ml of each antibody per 1 × 10⁶ cells and HA tetramer was the diluter at a ratio of 5 ml per 1 × 10⁶ cells. Splenocytes were isolated from a mouse spleen by immersing the spleen in Hanks' balanced salt solution (HBSS) with 10% FBS and washing with HBSS to remove blood. The spleen was placed in a 40-mm cell strainer and the tissue was mashed with a syringe plunger to break down the tissue and dislodge the cells. After complete disruption of the organ, the cells were run through the strainer into a conical tube. The cell suspension was pelleted by centrifugation at 350g for 10 min at 4 °C. The pellet was resuspended in water for 20 s to disrupt red blood cells followed by addition of 2 × PBS solution. The cells were pelleted and subjected to staining as described for PBMCs above.

Flow cytometry. After staining, the cells were fixed and subjected to flow cytometry using a BD LSR II flow cytometer (BD Biosciences) equipped with 488-nm, 405-nm, 640-nm and 532-nm lasers. Data were collected using BD FACSDiva software (BD Biosciences) and analyzed using FlowJo software (TreeStar). The gating strategy for positive tetramer cells was as follows: forward scatter area (FSC)-H/FSC-A gate used to collect cells and a gate for live cells was then generated. The live cells were gated for CD3⁺/CD45⁺ cells and the positive cells were gated to determine the CD8⁺/HA-tetramer⁺ cells. Acquired data was analyzed using a FlowJo software (TreeStar).

LNA effect on IFN and NF-κB pathways. THP1-Dual or A549-Dual cells (InvivoGen) were transfected in triplicate with LNA9, LNA14 or derivatives thereof, or poly(I:C) (R&D Systems) using Lipofectamine 2000 (Thermo Fisher Scientific) according to the manufacturer's protocol. Treatment with recombinant human tumor necrosis factor α (hTNF-α; R&D Systems), recombinant human IFN (hIFN-γ; R&D Systems), recombinant hIFN-α (R&D Systems) or lipopolysaccharide (LPS) from O111:B4 *Escherichia coli* (Sigma-Aldrich) was used as a positive control for activation of the two pathways. Supernatant from the cultures were collected 24–32 h post-transfection/treatment to measure luciferase signal or secreted alkaline phosphatase activity as indicators of IFN pathway

stimulation or NF- κ B pathway stimulation, respectively. Results were normalized to reflect fold induction relative to NT cells.

IL-6 and TNF- α ELISA. Supernatants from THP1-Dual cells (InvivoGen) were transfected in triplicate with LNA9, LNA14 or poly(I:C) (R&D Systems). Treatment with recombinant hIFN- γ (R&D Systems), recombinant hIFN- α (R&D Systems) or LPS from O111:B4 *E. coli* (Sigma-Aldrich) was used as a positive control to cause induction of interleukin (IL)-6 or TNF- α secretion. Supernatants were collected 24 h post-transfection/treatment and assayed for TNF- α and IL-6 concentration by ELISA (Thermo Fisher Scientific) according to the ELISA kit protocol.

Statistical analyses. We expressed the data as the mean \pm s.d. or mean \pm s.e.m. where indicated. We used Student's *t*-test (to compare two samples) or ANOVA (to compare multiple samples) as analyzed by GraphPad Prism (v.8 and v.9) for statistical analysis. We performed Kaplan–Meier log(rank) tests for survival analyses. We considered all *P* values >0.05 not to be significant.

Reporting summary. Further information on research design is available in the Nature Research Reporting Summary linked to this article.

Data availability

Data for 1D SHAPE experiment is available in source data of this manuscript. Chemical-mapping datasets for mutate-and-map and mutation/rescue experiments are available at <http://rmdb.stanford.edu>, accession nos. PSL2IAV_1M7_0001, PSL2IAV_RSQ_0001. Source data are provided with this paper. All the data that support the findings of the present study are available from the corresponding author upon request.

Code availability

DNA oligomers automated design script is available as MATLAB script at <https://primerize.stanford.edu>. A code to analyze map-and-mutate datasets is available as MATLAB script for download at <https://ribokit.github.io/HiTRACE>. A tutorial is available at <http://hitrace.org>. One-dimensional SHAPE with FAST algorithm embedded in the RNAstructure program is freely available at <http://med.stanford.edu/glennlab/download.html>.

References

- Hoffmann, E., Neumann, G., Kawaoka, Y., Hobom, G. & Webster, R. G. A DNA transfection system for generation of influenza A virus from eight plasmids. *Proc. Natl Acad. Sci. USA* **97**, 6108–6113 (2000).
- Hou, Y. J. et al. SARS-CoV-2 reverse genetics reveals a variable infection gradient in the respiratory tract. *Cell* **182**, 429–446.e414 (2020).
- Dinnon, K. H. 3rd et al. A mouse-adapted model of SARS-CoV-2 to test COVID-19 countermeasures. *Nature* **590**, E22 (2021).
- Szretter, K. J., Balish, A. L. & Katz, J. M. Influenza: propagation, quantification, and storage. *Curr. Protoc. Microbiol.* **Chapter 15**, Unit 15G, 11 (2006).
- Marsh, G. A., Hatami, R. & Palese, P. Specific residues of the influenza A virus hemagglutinin viral RNA are important for efficient packaging into budding virions. *J. Virol.* **81**, 9727–9736 (2007).
- Kawakami, E. et al. Strand-specific real-time RT-PCR for distinguishing influenza vRNA, cRNA, and mRNA. *J. Virol. Methods* **173**, 1–6 (2011).
- Mortimer, S. A. & Weeks, K. M. Time-resolved RNA SHAPE chemistry: quantitative RNA structure analysis in one-second snapshots and at single-nucleotide resolution. *Nat. Protoc.* **4**, 1413–1421 (2009).
- Akbari, A. et al. Improved DNA fragment length estimation in capillary electrophoresis. *Electrophoresis* **29**, 1273–1285 (2008).
- Deigan, K. E., Li, T. W., Mathews, D. H. & Weeks, K. M. Accurate SHAPE-directed RNA structure determination. *Proc. Natl Acad. Sci. USA* **106**, 97–102 (2009).
- De Rijk, P., Wuyts, J. & De Wachter, R. RnaViz 2: an improved representation of RNA secondary structure. *Bioinformatics* **19**, 299–300 (2003).
- Kladwang, W., VanLang, C. C., Cordero, P. & Das, R. A two-dimensional mutate-and-map strategy for non-coding RNA structure. *Nat. Chem.* **3**, 954–962 (2011).
- Kladwang, W., Cordero, P. & Das, R. A mutate-and-map strategy accurately infers the base pairs of a 35-nucleotide model RNA. *RNA* **17**, 522–534 (2011).
- Cordero, P., Kladwang, W., VanLang, C. C. & Das, R. The mutate-and-map protocol for inferring base pairs in structured RNA. *Methods Mol. Biol.* **1086**, 53–77 (2014).
- Mortimer, S. A. & Weeks, K. M. A fast-acting reagent for accurate analysis of RNA secondary and tertiary structure by SHAPE chemistry. *J. Am. Chem. Soc.* **129**, 4144–4145 (2007).
- Yoon, S. et al. HiTRACE: high-throughput robust analysis for capillary electrophoresis. *Bioinformatics* **27**, 1798–1805 (2011).
- Kim, H., Cordero, P., Das, R. & Yoon, S. HiTRACE-Web: an online tool for robust analysis of high-throughput capillary electrophoresis. *Nucleic Acids Res.* **41**, W492–W498 (2013).
- Kim, J. et al. A robust peak detection method for RNA structure inference by high-throughput contact mapping. *Bioinformatics* **25**, 1137–1144 (2009).
- Kladwang, W. et al. Standardization of RNA chemical mapping experiments. *Biochemistry* **53**, 3063–3065 (2014).
- Mathews, D. H. et al. Incorporating chemical modification constraints into a dynamic programming algorithm for prediction of RNA secondary structure. *Proc. Natl Acad. Sci. USA* **101**, 7287–7292 (2004).
- Darty, K., Denise, A. & Ponty, Y. VARNA: interactive drawing and editing of the RNA secondary structure. *Bioinformatics* **25**, 1974–1975 (2009).
- Cordero, P., Lucks, J. B. & Das, R. An RNA Mapping DataBase for curating RNA structure mapping experiments. *Bioinformatics* **28**, 3006–3008 (2012).

Acknowledgements

We thank H. Jin and her team at MedImmune for the kind donation of chicken eggs and technical guidance at the start of the project. We thank the Stanford in vitro BSL-3 Service Center and its director J. Garhyan for assistance with the SARS-CoV-2 research. We thank additional members of R.D.'s lab, I. N. Zheludev, R. Rangan and H. Wayment-Steele, for meaningful discussions of the SARS-CoV-2 structures and design of original SARS-CoV-2 RNA constructs for SHAPE experiments. The work was supported in part by a Mona M. Burgess Stanford BIO-X Interdisciplinary Graduate Fellowship (to R.J.H.), the National Institutes of Health (NIH) Graduate Training Grant (no. 5T32AI007328-24 to R.J.H.), NIH Training Grant (no. 5T32DK007056 to E.A.P.) and the following grants to J.S.G.: NIH research grants (nos. R56A1111460, U19A1109662, RO1A1132191 and U19A1171421), an influenza Harrington Scholar Innovator grant and grant no. W81XWH1810647 from the US Army Medical Research Acquisition Activity, Department of Defense, Open Philanthropy and Good Ventures Fund, Fastgrants, a COVID-19 Harrington Scholar Innovator Grant and the Dr. Tri Cao Nguyen Fund for Pandemic Preparedness. The work was also supported in part by the Intramural Research Program of the National Institute of Allergy and Infectious Diseases, NIH. The data presented in this manuscript are tabulated in the main paper and the supplementary materials. Chemical-mapping datasets for M² and M²R experiments have been deposited at the RMDb (<http://rmdb.stanford.edu>).

Author contributions

R.J.H. and J.S.G. conceived and designed the study. R.J.H., M.E., L.B., M.R., C.B.S., T.P.S., F.R.M., R.M.M., A.B., K.N. and S.T. performed the experiments. R.J.H., M.E., L.B., S.T., T.P.S. and C.B.S. analyzed the data. M.E., L.B., M.Y. and T.A. assisted with mouse experiments. E.A.P. and R.J.H. conceived the idea of targeting PSL2 and SARS-CoV-2-conserved RNA secondary structure using LNAs and designed antisense oligonucleotides. R.J.H., E.A.P. and M.E. designed LNA experiments and coordinated in vitro and in vivo SARS-CoV-2 experiments. B.F. performed sequencing and assisted in experimental prep. M.Y. and E.A.P. designed the in vitro assessment of LNAs in myeloid cells and M.Y. performed the experiments. J.D. and G.L. assisted in pharmacokinetics determination. P.L. assisted in cloning of IAV control constructs. W.K. provided important technical assistance on SHAPE experiments. A.X. assisted with experimental prep. P.S.P. contributed to the initial conception of the study. T.P.S., F.R.M. and R.M.M. assisted with SARS-CoV-2 experiments. A.R. and C.A.B. established the BSL-3 screening. A.R. performed the screening. C.J.F. isolated and characterized the SARS-CoV-2 clinical variant. B.L.H. managed the SARS-CoV-2 hamster study. S.A.G. performed the virus titrations. S.S. and P.K. provided bioinformatics and statistical analyses. C.T. was instrumental in setting up in vivo SARS-CoV-2 assays and conditions. J.K.T. offered valuable expertise and coordinates before publication, discussed results and provided critical reagents. R.D. and J.S.G. provided experimental feedback and assisted in the analysis of the results. R.J.H., J.S.G., M.E., E.A.P., S.T. and R.D. wrote the paper.

Competing interests

J.S.G., R.J.H., E.P. and M.E. are inventors on patents pertaining to the materials presented in this article that has been filed with the US Patent and Trademark Office by Stanford University.

Additional information

Supplementary information The online version contains supplementary material available at <https://doi.org/10.1038/s41591-022-01908-x>.

Correspondence and requests for materials should be addressed to Jeffrey S. Glenn.

Peer review information *Nature Medicine* thanks the anonymous reviewers for their contribution to the peer review of this work. Primary Handling Editor: Alison Farrell, in collaboration with the *Nature Medicine* team.

Reprints and permissions information is available at www.nature.com/reprints.

Reporting Summary

Nature Research wishes to improve the reproducibility of the work that we publish. This form provides structure for consistency and transparency in reporting. For further information on Nature Research policies, see our [Editorial Policies](#) and the [Editorial Policy Checklist](#).

Statistics

For all statistical analyses, confirm that the following items are present in the figure legend, table legend, main text, or Methods section.

n/a Confirmed

- The exact sample size (n) for each experimental group/condition, given as a discrete number and unit of measurement
- A statement on whether measurements were taken from distinct samples or whether the same sample was measured repeatedly
- The statistical test(s) used AND whether they are one- or two-sided
Only common tests should be described solely by name; describe more complex techniques in the Methods section.
- A description of all covariates tested
- A description of any assumptions or corrections, such as tests of normality and adjustment for multiple comparisons
- A full description of the statistical parameters including central tendency (e.g. means) or other basic estimates (e.g. regression coefficient) AND variation (e.g. standard deviation) or associated estimates of uncertainty (e.g. confidence intervals)
- For null hypothesis testing, the test statistic (e.g. F , t , r) with confidence intervals, effect sizes, degrees of freedom and P value noted
Give P values as exact values whenever suitable.
- For Bayesian analysis, information on the choice of priors and Markov chain Monte Carlo settings
- For hierarchical and complex designs, identification of the appropriate level for tests and full reporting of outcomes
- Estimates of effect sizes (e.g. Cohen's d , Pearson's r), indicating how they were calculated

Our web collection on [statistics for biologists](#) contains articles on many of the points above.

Software and code

Policy information about [availability of computer code](#)

Data collection No software for data collection was used.

Data analysis MATLAB scripts for designing and analyzing mutate-and-map, mutate-and-rescue, and SARS-CoV-2 SHAPE datasets is available on https://github.com/DasLab/NA_thermo
MATHLAB R2021a, Prism9, RNAstructure v5.2, Instructions for download and installation of FAST algorithm with RNA structure are available at <https://med.stanford.edu/glennlab/download.html>
The HiTRACE software package version 2.0 was used to analyze CE data (both MATLAB toolbox and web server available) and can be found at <https://github.com/ribokit/HiTRACE>

For manuscripts utilizing custom algorithms or software that are central to the research but not yet described in published literature, software must be made available to editors and reviewers. We strongly encourage code deposition in a community repository (e.g. GitHub). See the Nature Research [guidelines for submitting code & software](#) for further information.

Data

Policy information about [availability of data](#)

All manuscripts must include a [data availability statement](#). This statement should provide the following information, where applicable:

- Accession codes, unique identifiers, or web links for publicly available datasets
- A list of figures that have associated raw data
- A description of any restrictions on data availability

Chemical mapping datasets for mutate-and-map and mutation/rescue experiments are available at <http://rmdb.stanford.edu>80, accession codes:

Field-specific reporting

Please select the one below that is the best fit for your research. If you are not sure, read the appropriate sections before making your selection.

Life sciences Behavioural & social sciences Ecological, evolutionary & environmental sciences

For a reference copy of the document with all sections, see [nature.com/documents/nr-reporting-summary-flat.pdf](https://www.nature.com/documents/nr-reporting-summary-flat.pdf)

Life sciences study design

All studies must disclose on these points even when the disclosure is negative.

Sample size	No sample size was statistically predetermined. Given the reproducibility of cell culture experiments, it was predetermined that a minimum of at least n=2 would provide sufficient information to reach meaningful data conclusions. Where possible, in vitro sample size was n=3 or more. For in vivo experiments the number of animals per group in IAV experiments with BALB/c mice was determined using G*power statistical software with the following parameters: Effect size- 1.8; Power- 90%, Type 1 error- and determined to be 7. For SARS-COV-2 animal experiment power was reduced to 80% and was acceptable considering the short supply of hamsters, group size was determined to be 5.
Data exclusions	No data was excluded in this manuscript.
Replication	Experiments herein underwent multiple replication studies, depending on the nature of the experiment (in vitro vs in vivo), and all replication attempts were successful. Influenza animal studies were replicated at least twice, SARS-CoV-2 animal studies were performed once. In instances where higher variability resulted, an increased number of replicates was employed to assure findings. All SARS-CoV-2 studies performed in BSL3 (in vitro and in vivo) performed only once with multiple biological replicates due to limited access to these facilities.
Randomization	All mouse studies were randomized. We assigned equal number of mice randomly into each group. Weights were determined only after assignment to groups and prior to infection.
Blinding	Animal experiments were randomized blindly. The investigator was conducting the experiments, therefore data collection and analysis could not be blinded.

Reporting for specific materials, systems and methods

We require information from authors about some types of materials, experimental systems and methods used in many studies. Here, indicate whether each material, system or method listed is relevant to your study. If you are not sure if a list item applies to your research, read the appropriate section before selecting a response.

Materials & experimental systems

Methods

n/a	Involved in the study	n/a	Involved in the study
<input type="checkbox"/>	<input checked="" type="checkbox"/> Antibodies	<input checked="" type="checkbox"/>	<input type="checkbox"/> ChIP-seq
<input type="checkbox"/>	<input checked="" type="checkbox"/> Eukaryotic cell lines	<input type="checkbox"/>	<input checked="" type="checkbox"/> Flow cytometry
<input checked="" type="checkbox"/>	<input type="checkbox"/> Palaeontology and archaeology	<input checked="" type="checkbox"/>	<input type="checkbox"/> MRI-based neuroimaging
<input type="checkbox"/>	<input checked="" type="checkbox"/> Animals and other organisms		
<input checked="" type="checkbox"/>	<input type="checkbox"/> Human research participants		
<input checked="" type="checkbox"/>	<input type="checkbox"/> Clinical data		
<input checked="" type="checkbox"/>	<input type="checkbox"/> Dual use research of concern		

Antibodies

Antibodies used

mouse anti-HA, Sinbiological, HB09AU0402-B (1:800); rabbit anti-PB2, Invitrogen PA5-3221 (1:1000); H-2Kd Influenza HA Tetramer-IYSTVASSL-PE, MBL International, TB M520-1 (5 micro liter per 1x 10e6 cells); APC/Cy7 anti-mouse CD8a, Biolegend, 100714 (2 micro-liter per 1x 10e6 cells); PE/Cy7 anti-mouse CD3, Biolegend, 100220 (2 micro-liter per 1x 10e6 cells); BD Horizon™ PE-CF594 Rat Anti-Mouse CD45, BD biosciences, 562420 (2 micro-liter per 1x 10e6 cells);Zombie Aqua™ Fixable Viability Kit, Biolegend, 423102 (1:500); Anti-Rabbit HRP (ThermoFisher, 65-6120); Goat-anti-Rabbit Alexa-Flour 488 (ThermoFisher, A-11008); mouse Anti-Actin (Sigma A2228)

Validation

Antibodies were purchased from Sinbiological, Invitrogen, MBL international, Biolegend, BD biosciences, ThermoFisher and Sigma. Validation information is available from the manufacturers who provide references on their websites for the catalogue number listed above. See <https://www.biolegend.com/> for Biolegend, <https://www.thermofisher.com> for Invitrogen and ThermoFisher, <https://www.sigmaldrich.com/> for Sigma, <https://www.bdbiosciences.com/> for BD Biosciences, and <https://>

Eukaryotic cell lines

Policy information about [cell lines](#)

Cell line source(s)	MDCK- NBL2 (ATCC, CCL-34), HEK 293T (ATCC CRL-1573), VeroE6 (ATCC CRL-1586) Huh7.5_TMPRSS-ACE2 and A549-ACE2 (A gift from Dr. Timothy Sheahan); A549(ATCC, CCL-185); ATCC, A549-Dual (InvivoGen, a549d-nfis); THP1-Dual (InvivoGen, thpd-nfis)
Authentication	Cell lines were purchased from vendors and were not authenticated further. Huh7.5_TEMPRSS-ACE2 and A549-ACE2 were generated by Dr. Sheahan and were not authenticated further.
Mycoplasma contamination	All cell lines were tested negatively for mycoplasma contamination.
Commonly misidentified lines (See ICLAC register)	no commonly misidentified cell lines were used in this study

Animals and other organisms

Policy information about [studies involving animals](#); [ARRIVE guidelines](#) recommended for reporting animal research

Laboratory animals	BALB/c female mice, 6-8 weeks old (Jackson Laboratories) Golden Syrian Hamsters strain LVG, 10 week old females (Charles River) Specific-pathogen-free chicken embryos (Charles River)
Wild animals	No wild animals were used in the study.
Field-collected samples	No field collected samples were used in the study.
Ethics oversight	Stanford University Administrative Panel on Laboratory Animal Care, Utah State University IACUC

Note that full information on the approval of the study protocol must also be provided in the manuscript.

Flow Cytometry

Plots

Confirm that:

- The axis labels state the marker and fluorochrome used (e.g. CD4-FITC).
- The axis scales are clearly visible. Include numbers along axes only for bottom left plot of group (a 'group' is an analysis of identical markers).
- All plots are contour plots with outliers or pseudocolor plots.
- A numerical value for number of cells or percentage (with statistics) is provided.

Methodology

Sample preparation	Whole blood was collected from mice into heparinized tubes. The whole blood was overlaid on top Ficoll-Paque media and centrifuged at 400xg for 40 minutes at room temperature. The top layer containing plasma and platelets was removed and the peripheral blood mono-nuclear cells (PBMCs) at the interphase of the Ficoll layer were collected. The mononuclear cells were diluted in PBS and pelleted by centrifugation at 500 x g for 15 minutes following an additional wash with PBS. The pellet was suspended in PBS. Solenocytes were isolated by manual grinding of the spleen over a 40 µm cell strainer. The cells were transferred several times through the strainer and processed further as described above.
Instrument	BD bioscience LSR II , see Online Methods
Software	Data was collected using the BD FACSDiva software (BD biosciences) and analyzed using FlowJo v10
Cell population abundance	Percent of cell population is presented in Supplemental figure 18
Gating strategy	FSC-H/FSC-A gate used to collect cells and a gate for live cells was then generated. The live cells were gated for CD3+/CD45+ cells and the positive cells were gated to determine the CD8+/HA-Tetramer+ cells. The gating strategy is exemplified in source data for Supplemental Figure 18

- Tick this box to confirm that a figure exemplifying the gating strategy is provided in the Supplementary Information.